UPPSALA
UNIVERSITET

Digital Comprehensive Summaries of Uppsala Dissertations from the Faculty of Science and Technology 631

Fabrication of Electroacoustic Devices for Integrated Applications

JOHANNES ENLUND

ACTA
UNIVERSITATIS
UPSALIENSIS
UPPSALA
2009

ISSN 1651-6214
ISBN 978-91-554-7487-4
urn:nbn:se:uu:diva-100381

Dissertation presented at Uppsala University to be publicly examined in Siegbahnsalen, Ångström laboratory, Uppsala, Friday, May 15, 2009 at 09:30 for the degree of Doctor of Philosophy. The examination will be conducted in English.

Abstract
Enlund, J. 2009. Fabrication of Electroacoustic Devices for Integrated Applications. Acta Universitatis Upsaliensis. *Digital Comprehensive Summaries of Uppsala Dissertations from the Faculty of Science and Technology* 631. 70 pp. Uppsala. ISBN 978-91-554-7487-4.

Electroacoustic technology has in many ways revolutionised the wireless telecommunication industry. The IC compatible fabrication technique of thin film electroacoustic devices has so far provided a considerable increase in device performance and reduction in size. At the moment, new areas where this technology can be of use is under investigation. In particular, thin film bulk acoustic wave resonators are promising candidates for biochemical and gravimetric sensor applications.

For bulk acoustic waves, the thesis addresses a number of aspects in the design, fabrication, characterisation, and integration of thin film electroacoustic devices. The object of the studies conducted in the thesis has been to improve on design and thereby optimise the performance of the device to fit a particular application of interest. For high frequency and high power applications, a conceptually new design of the solidly mounted resonator has been investigated. A 1 GHz plate wave resonator with a much higher Q factor than its surface acoustic counterpart have also been fabricated. A multi-chip-module 2 GHz microwave oscillator featuring a monolithically integrated solidly mounted resonator and a flip chip transistor have been fabricated and characterised with a phase noise of -125 dBc/Hz at 100 kHz. For sensor applications, the fabrication of shear mode solidly mounted resonators featuring c-axis inclined AlN films has been studied. A process for the bonding of a microfluidic system on top of the resonator has been realised. Further, the effect of conductive liquids on the resonator performance has been investigated.For surface acoustic wave devices, acoustic manipulation of particles in microfluidic channels has been studied. Two functional devices have been fabricated by bonding piezoelectric substrates to glass or fused silica superstrates. By generating an interface acoustic wave, that propagates along the bonded interface, manipulation of sub-micrometer particles was realised.

Keywords: piezoelectric resonators, bulk acoustic wave devices, surface acoustic wave devices, interdigital transducers, biomedical transducers, microwave oscillators, sensor, aluminum nitride, reactive sputtering

Johannes Enlund, Department of Engineering Sciences, Box 534, Uppsala University, SE-75121 Uppsala, SwedenSolid State Electronics, Box 534, Uppsala University, SE-75121 Uppsala, Sweden

ISSN 1651-6214
ISBN 978-91-554-7487-4
urn:nbn:se:uu:diva-100381 (http://urn.kb.se/resolve?urn=urn:nbn:se:uu:diva-100381)

Shine on you crazy diamond.

List of Appended Papers

This thesis is based on the following papers, which are referred to in the text by their Roman numerals.

I J. Enlund, D.M. Martin, V. Yantchev, and I. Katardjiev, Solidly mounted thin film electro-acoustic resonator utilizing a conductive Bragg reflector, *Sensors & Actuators: A. Physical*, Vol 141, No 2, pp 598 - 602, 2008

II V. Yantchev, J. Enlund, J. Bjurström, and I. Katardjiev, Design of high frequency piezoelectric resonators utilizing laterally propagating fast modes in thin aluminum nitride (AlN) films, *Ultrasonics*, Vol 45, No 1-4, pp 208 - 12, 2006

III J. Enlund, V. Yantchev, and I. Katardjiev, Electric field sensitivity of thin film resonators based on piezoelectric AlN thin films, *IEEE Ultrasonics Symposium 2006*, pp 468-471, 2006

IV D.M. Martin, J. Enlund, V. Yantchev, U. Smith, J. Olsson, and I. Katardjiev, Thick silicides synthesised with smooth surface for integrated TFBAR applications, Submitted to *Journal of Micromechanics and Microengineering.*

V M. Norling, J. Enlund, S. Gevorgian, and I. Katardjiev, A 2 GHz oscillator based on a solidly mounted thin film bulk acoustic wave resonator, *IEEE MTT-S International Microwave Symposium Digest*, pp 1813 - 1816, 2006

VI M. Norling, J. Enlund, I. Katardjiev, and S. Gevorgian, Oscillators based on monolithically integrated AlN TFBARs, *IEEE Transactions on Microwave Theory and Techniques*, Vol 56, No 12, pp 3209 - 16, 2008

VII G. Sharma, L. Liljeholm, J. Enlund, J. Bjurström, I. Katardjiev, and K. Hjort, Fabrication and characterization of a shear mode AlN solidly mounted resonator-silicone microfluidic system for in-liquid sensor applications, Submitted to *Sensors & Actuators: A. Physical*

VIII J. Enlund, D.M. Martin, V. Yantchev, and I. Katardjiev, Q-degradation and crosstalk in BAW sensor arrays operating in conductive liquid media, Submitted to *IEEE Sensors*.

IX J. Enlund, L. Johansson, S. Johansson, I. Katardjiev, and V. Yantchev, Surface acoustic wave-excited particle manipulation in a glass microfluidic channel, Submitted to *Journal of Micromechanics and Microengineering*.

X V. Yantchev, J. Enlund, I. Katardjiev, S. Johansson, and L. Johansson, Interface acoustic wave based particle manipulation in microfluidic channels, Submitted to *Lab on a Chip*.

Reprints were made with permission from the publishers.

Contents

1. Introduction

Since the early 20th century, electroacoustic (EA) devices utilising the piezoelectric effect, discovered by Pierre Curie in 1880, have found their use in a multitude of components such as signal filters, delay lines, resonators, oscillators, sensors, and actuators. Today, most of these devices are found in telecommunication applications.

The most commonly used materials are bulk single crystalline piezoelectric materials, such as Quartz (SiO2), $LiNbO_3$, and $LiTaO_3$. During the last thirty years, however, the proliferation of more sophisticated deposition tools, have enabled the realisation of electroacoustic devices based on thin film technology and polycrystalline piezoelectric materials such as zinkoxode (ZnO), and aluminiumnitride (AlN).

In recent years, the field where EA technology has had its largest impact, is wireless communication applications consuming more than four billion filters annually. Ever since the mobile telephone became every day's commodity, the market has demanded increased functionality, including Bluetooth, FM radio, GPS, WiFi, and TV receivers, all of which are packed within the limited volume of the mobile phone in the palm of your hand. The ability to fit all these different RF modules within the confined space of the phone, has meant a remarkable reduction in device footprint in addition to improved performance. A recent investigation showed that the RF front-end, including the duplex filter of the early phones was more than 100 times the weight and volume of their modern equivalent [1].

In light of the RF-front end story of success, a lot of research effort is put into finding new areas where the electroacoustic technology can be put to use. In particular, since these devices are fabricated using integrated circuit (IC) compatible processes, the integration of EA and IC components have been on the agenda for some time. Here technologies such as multi-chip-module (MCM), Above-IC and Flip-Chip technologies are the most prominent.

Another interesting field, focus on utilising thin film resonators in sensor applications. As a sensor, the resonance frequency shift that can be observed due to the mass loading effect of the resonator, can be used to detect the presence of minute volumes of molecular species.

This thesis covers the design, fabrication and characterisation of electroacoustic devices used in a wide range of applications including resonators, oscillators, sensors, and devices used for microparticle manipulation. The main part of the devices rely on bulk acoustic wave (BAW) excitation and are based on reactively sputtered polycrystalline aluminiumnitride (AlN) (Papers I - VIII). The devices fabricated on bulk piezoelectric substrates (Papers IX and

X) are based on surface acoustic wave excitation. They have been fabricated in the clean room facility at the Ångström laboratory in Uppsala.

In this introductory chapter a basic theory of electroacoustics is presented. First, the propagation of acoustic waves in piezoelectric solids is covered. Then, the conversion between electrical and mechanical energy is discussed. For simplicity, only the one dimensional case is treated, but the theory can easily be expanded into three dimensions. For a more extensive treatment of the theory, the reader is referred to the literature [2, 3].

In the last section of this chapter, the process technology that have enabled the recent advances within thin film electroacoustics is presented.

1.1 Acoustic waves in solids

An acoustic wave propagating in a solid material is the result of small relative displacements of the particles that constitute the material. If an external force is momentarily applied to a material, it's constituent particle are displaced from their equilibrium position and the material is said to be "strained". Consequently, a restoring force referred to as "stress", is trying to put the particles back in their original position. If the stress is assumed to be elastic, the inertia of the particle will then bring it into an oscillatory motion.

There exist two basic types of bulk waves. The first is the longitudinal wave, in which the oscillations of the particles are only in the direction of the wave propagation. The second is the shear wave, in which the particle displacements are orthogonal to the wave propagation. The principle of longitudinal and shear wave propagation is pictured is Figure 1.1.

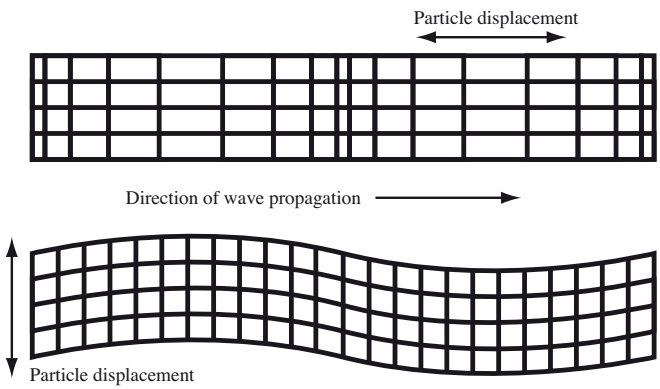

Figure 1.1: Material deformation for longitudinal (top) and shear (bottom) waves

If the particle displacements are small, the coupling between the stress (T) and the strain (S) can be defined by the linear relation $T = CS$, also referred to as Hooke's law, where C is the stiffness constant of the material. For the same material, the electrical displacement is defined as $D = \varepsilon E$, where E is the

electric field and ε the permittivity. With the assistance of Newton's second law $F = ma$, Hooke's law can be written in the form of a wave equation.

$$\frac{1}{\rho}\frac{\partial^2 T}{\partial z^2} = \frac{1}{C}\frac{\partial^2 T}{\partial t^2} \tag{1.1}$$

The solution to the wave equation, is a plane wave propagating in the material with a constant phase and amplitude on any plane perpendicular to the direction of propagation. The particle velocity v in the material is given by

$$v = \frac{1}{\sqrt{\rho C}}T. \tag{1.2}$$

The reciprocal $\sqrt{\rho C}$ is the characteristic acoustic impedance z and is an important material property as will be explained later on. The particle velocity should not be confused with the phase velocity v_{ph} given by

$$v_{ph} = \sqrt{\frac{C}{\rho}}, \tag{1.3}$$

where ρ is the density of the material.

In an isotropic material, the phase velocity of the acoustic wave does not change with the direction of propagation. Since any particular direction of propagation will give rise to the same stress and strain relation, only pure modes, one longitudinal and two shear modes, can exist in the material. Each of these associated with its acoustic phase velocity and polarisation. In anisotropic materials, however, the propagation characteristics of an acoustic wave is strongly dependent on the propagation direction and the symmetry class of the material. Consequently, both pure modes and "quasi" modes can exist. The quasi-longitudinal wave is polarised mainly in the direction of propagation while the quasi shear wave is polarised mainly perpendicular to the direction of propagation.

1.1.1 Piezoelectricity

In a piezoelectric material the mechanical properties defined by stress and strain are coupled to the electrical properties. If the material is deformed by, e.g. an external force, the particle displacements produces small local dipoles which may for certain materials combine to produce a macroscopic electrical polarisation of the material. This phenomenon is also called the direct piezoelectric effect, which for small signal analysis can be considered to be linear. Accompanying direct piezoelectric effect, is the converse piezoelectric effect whereby the material will become deformed or strained in the presence of an external electric field.

In order to compensate for the strain generated in a piezoelectric solid by such an external electric field, Hooke's law and the displacement relation are modified by adding a piezoelectric terms that are linearly proportional to the

electric field and the strain:

$$T = C^E S - eE, \tag{1.4}$$

$$D = eS + \varepsilon E, \tag{1.5}$$

where e is the piezoelectric constant and C^E is referred to as the "stiffened" stiffness constant and the superscript E denotes that the stiffness constant is measured at constant electric field. Together, Equations 1.4 and 1.5 form the constitutive relations. Because of the piezoelectric correction term, the phase velocity of acoustic waves are always higher in a piezoelectrically active material than in non-piezoelectric media and we have for the stiffened phase velocity

$$v'_{ph} = \sqrt{\frac{C^E}{\rho}\left(1 + \frac{e^2}{\varepsilon^S C^E}\right)}, \tag{1.6}$$

where ε^S is the electric permittivity at constant strain. Writing 1.6 in terms of 1.3, we get

$$v'_{ph} = v\sqrt{1 + \frac{e^2}{\varepsilon^S C^E}} = v\sqrt{1 + K^2}. \tag{1.7}$$

A more popular name for the piezoelectric correction term K^2 in 1.7 is the piezoelectric coupling constant. This is an important parameter since, in the piezoelectric crystal, electric energy is converted into mechanical energy, and vice versa. A simple interpretation of K^2 is the ratio of electric field energy to mechanical energy density. If the acoustically generated electric field is in the direction of the acoustic wave propagation, we define the electromechanical coupling constant as

$$k_t^2 = \frac{K^2}{1 + K^2}. \tag{1.8}$$

1.1.2 Material properties

The piezoelectric material used in the electroacoustic devices featured in this thesis, are based on thin film aluminium nitride (AlN). The table in this section summarises some of the material parameters of aluminium.

Table 1.1: *Material constants of aluminium nitride [4, 5]*

Parameter	Symbol	Value	Unit
Density	ρ	3260	[kg/m^3]
Elastic stiffness	C_{11}	3.45	10^{11} N/m^2
	C_{12}	1.25	10^{11} N/m^2
	C_{13}	1.20	10^{11} N/m^2
	C_{33}	3.95	10^{11} N/m^2
	C_{44}	1.18	10^{11} N/m^2
	C_{66}	1.10	10^{11} N/m^2
Piezoelectric constant	e_{15}	-0.48	C/m^2
	e_{31}	-0.58	C/m^2
	e_{33}	1.55	C/m^2
Dielectric constant	ε_{11}	8.0	10^{-11} F/m
	ε_{33}	9.5	10^{-11} F/m
Thermal expansion	α_{11}	5.27	10^{-6} K^{-1}
	α_{11}	4.15	10^{-6} K^{-1}

1.2 Process technology

This section summarises the process techniques used in the fabrication of the electroacoustic devices featured in this thesis.

1.2.1 Physical vapour deposition

Physical vapour deposition (PVD) is a family name for the deposition of thin films by the condensation of a vaporised material on a surface, e.g. a layer of Al on a Si substrate. These methods use purely physical processes, such as high temperatures or ion bombardment to generate the material vapour from solid sources and require vacuum conditions.

Sputtering

Sputter deposition, or sputtering is a technique frequently used by the semiconductor industry for the deposition of thin films over large areas. The process offers many advantages over other techniques such as excellent film uniformity, high deposition rates, and conformal or planarised coatings. More-

over, sputtering is a versatile process and almost any material that can be introduced in a vacuum system and be sputter deposited.

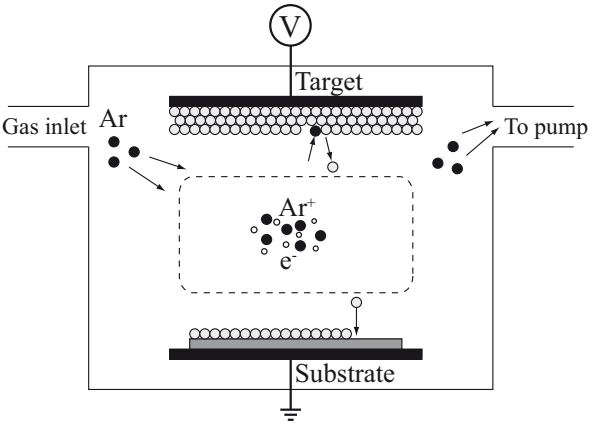

Figure 1.2: Simple schematic of a DC sputter system.

In sputtering the material vapour is created from a solid source by the bombardment of energetic ions. Fig. 1.2 shows a simple schematic of a DC sputter system. The process chamber, which is evacuated by a turbo molecular pump, houses a cathode and an anode connected to an external power supply. With the chamber evacuated, a gas is introduced into the system at pressures around 1 to 100 mTorr. The electric field between the anode and cathode will accelerate negative and positive charges stochastically present in the gas. An electron that ionises an atom during a collision according to $e^- + Ar = Ar^+ + 2e^-$, will result in an avalanche effect and the establishment of a plasma between the cathode and anode. The ions are accelerated towards the cathode which they hit with a high kinetic energy.

For thin film deposition, the material to be deposited (target) is attached to the cathode, and the substrate is placed on the anode. The positive ions created in the plasma strike the target at high energy resulting in the physical removal of target atoms and secondary electrons from the target surface. These neutral atoms now travel away from the target through the plasma and condense onto the substrate surface, while the secondary electrons contribute to the ionisation process in the plasma and maintain the discharge.

Reactive sputtering

In reactive sputtering, the deposited film is formed by chemical reaction between the target material and the gas which is introduced into the process chamber. This process is particularly useful when depositing oxide and nitride thin films. If, for example the target material is Al and the process gases in the chamber is Ar and N_2, the sputtered atoms will react with the reactive N_2 molecules and thereby form a thin AlN film.

Evaporation

Evaporation uses a high temperature and low pressure to produce the deposition vapour. Thin films of Al, Cu, Au, Ti, and Cr are often deposited using this technique. For resistive evaporation, the material is placed in a tungsten crucible. An electrical current led through the crucible heats it up such that the material will melt and evaporate. For some materials with high melting temperatures like Ti and Cr, sublimation occurs. Like sputtering, evaporation takes place in vacuum, i.e. vapours other than the material are removed from the process chamber by a pump. In vacuum (with a long mean free path), evaporated particles can travel directly to the deposition substrate without colliding with the background atmosphere. Since material is vaporised from a point source, poor step coverage is a characteristic of evaporated films. A simple schematic of an evaporator system is shown in Fig. 1.3 with both resistive and e-beam material sources.

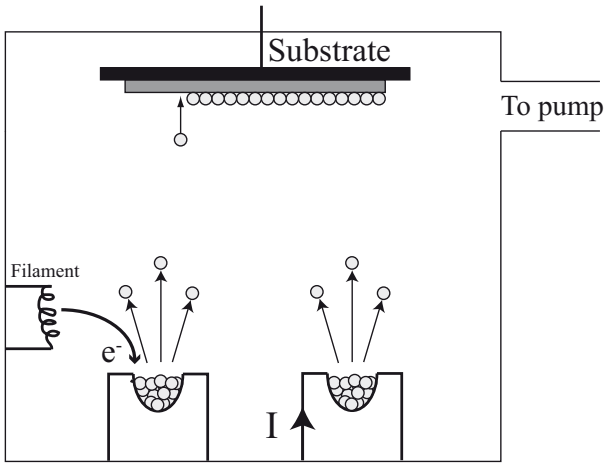

Figure 1.3: Simple schematic of a multi source evaporator system. The crucible to the left is the e-beam source and the crucible to the right is the resistive source.

Electron-beam evaporation

In e-beam evaporation, the crucible is bombarded with an electron beam given off by a charged tungsten filament under high vacuum conditions. The electron beam causes the material to heat up and transform into the gaseous phase.

1.2.2 Chemical vapour deposition

Chemical vapour deposition (CVD) is a family name for the deposition of high-purity solid materials from one or more volatile precursors. Silicondioxide (SiO_2) can for example be deposited from a silane SiH_4 precursor, which undergoes the following reaction: $SiH_4(G) + O_2(G) = SiO_2(S) + 2H_2(G)$. This reaction occurs around 500°C, and the by-products are removed from

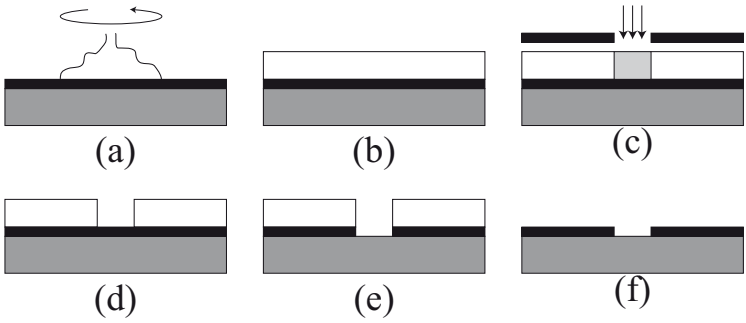

Figure 1.4: Process steps for patter replication using photolithography. Resist is applied to the substrate (a)and a thin film is defined by spinning the substrate (b). The desired pattern is transferred to the resist by UV exposure (c) and the exposed areas subsequently removed by basic developer solution (d). The thin film can now be etched (e) after which the resist is removed (f).

the system by pumps. CVD processes are commonly used in semiconductor fabrication for depositing thin metal and dielectric films such as Mo, W, polycrystalline-Si, diamond, and SiN.

In this work, a plasma enhanced CVD (PECVD) process has been used to deposit thin SiO_2 films. The plasma provides energy to the reaction given above and is thus able to reduce the temperature at which the reaction occurs to less than 300°C. This is particularly important for back-end passivation of wafers with metal layers already defined on the substrate.

1.2.3 Photolithography

Photolithography is a very sophisticated pattern replication process used in microfabrication for the selective removal or deposition of a thin film on to a particular substrate. The geometric pattern is predefined in a photomask and is transferred to the substrate via a light sensitive polymer, called photoresist (resist). The basic steps are illustrated in Fig. 1.4. The liquid phase resist is applied onto the deposited film by spinning the substrate at high speed, producing a uniform coating. The resist is then hardened in a baking step that removes all of the solvents from the material. Next, the resist is exposed through the photomask using a UV-light source. For a positive resist, the exposed areas become soluble in the basic developer and can thus be removed from the substrate. The exposed areas of the film can now be etched. Finally, the resist is removed using acetone solvent. The substrate is now ready for the next process step.

If no suitable etch process is available for the deposited film, a technique called "lift-off" can be used. In this process, the resist is deposited and patterned prior to film deposition. Then the substrate is immersed in an ultrasonic acetone bath which removes the resist and excess film material.

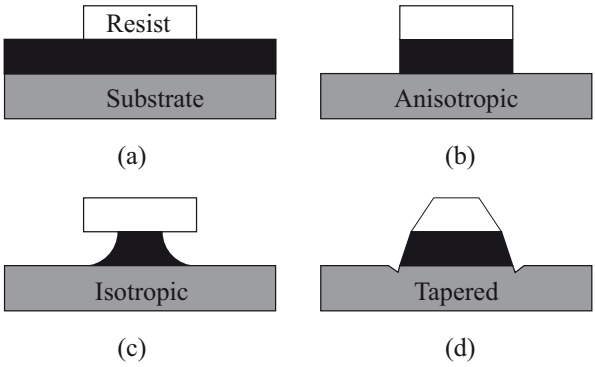

Figure 1.5: Etch profiles. (a) The replicated pattern is defined by a layer of photoresist. (b) If the etch is anisotropic vertical sidewalls and minimal loss of resolution is achieved. (c) If the etch rate is the same in all directions, the profile is circular. (d) Limited etch selectivity between the mask/film/substrate can produce tapered etch profiles and cause substrate damage.

1.2.4 Etching

The next cornerstone of microfabrication is etching. During this process, exposed areas on the substrate, as defined in the previous section and Fig. 1.5(a), are removed. The etching mechanism is either a physical or a chemical process (or a combination of the two). Etch processes fall into two major categories: dry and wet etching. Dry etching involves reactions on the surface by a reactive species in a gaseous phase and bombardment from energetic ions generated by a plasma. During wet etching, the substrate is immersed into a liquid etchant that reacts with the exposed film.

One of the most important characteristics of film etching is the selectivity of the etchant with respect to the etch mask and underlying layer. The etch mask must be able to withstand the process environment without attaining any significant geometrical alterations, otherwise a loss in the pattern resolution is inevitable. An schematic example of mask erosion during dry etching is shown in Fig. 1.5 (d), where the consumption of the resist mask results in a tapered etch of the film.

Another important factor is the critical dimension (CD) which is defined as the minimum feature size that the etch/lithography process can produce. Unless the film thickness is much smaller than the width of the mask pattern, a substantial loss in mask resolution is inevitable if the etch does not exhibit a certain degree of anisotropy. The latter can be achieved with dry etch methods by ion bombardment and the passivation of vertical etch structures. In wet etching the chemicals may etch certain crystal planes preferentially. Isotropic and anisotropic etching is schematically illustrated in Fig, 1.5 (b) and (c).

For BAW devices such as the FBAR or SMR featured in this thesis, the critical dimension of the structures are on the order of tens or hundreds of micrometers, for which reason loss of linewidth is generally insignificant. For

FPAR and SAW devices, however, the precise definition of the IDTs are of vital importance as the line width influences both the metallisation ratio and the reflectivity of the fingers. Consequently, dry etch, or lift-off techniques are recommended for such devices depending on the choice of metallisation.

2. Thin film electroacoustic devices

In this chapter, an overview of the EA devices considered in this thesis is presented. For each device a brief description of the work done is also given.

A thin film bulk acoustic resonator (TFBAR) consists of a piezoelectric thin film sandwiched between two thin electrodes. If a low frequency signal is applied to the electrodes the impedance of the device will behave like a capacitor. If the frequency of the applied signal is increased to the point where the wavelength of the mechanical waves (generated through the reverse piezoelectric effect) is twice that of the film thickness, a standing wave is established between the outer boundaries of the electrodes and the device resonates. This is the lowest frequency that can be excited and is referred to as the fundamental resonance frequency, the TFBAR structure can, however, be used to excite any odd multiple of the $\lambda/2$ condition. If material is added to either side of the resonance cavity, e.g. a layer of SiO_2 for temperature compensation, even multiples can be excited [6].

Although AlN based electroacoustic devices are IC-compatible, they do not necessarily require the use of Si for their fabrication.

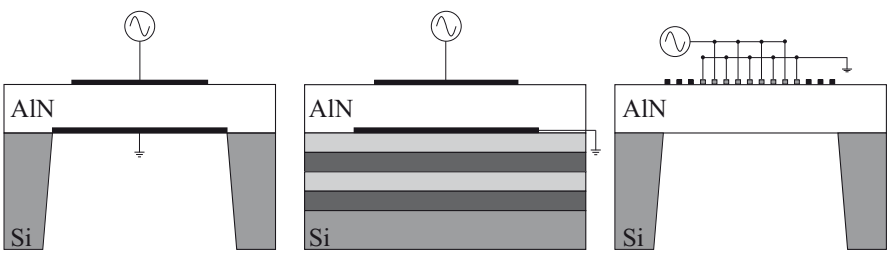

Figure 2.1: Schematic cross sections of the three types of electroacoustic devices featured in this thesis.

2.1 FBAR

As depicted in Fig. 2.1, the BAW resonators fabricated in this thesis, have three different designs. The leftmost device, (a) is the Film Bulk Acoustic Resonator (FBAR) which is featured in Paper III and IV. In the FBAR, acoustic isolation from the substrate is obtained by removing the substrate underneath the device. This is done by Deep Reactive Ion Etching (DRIE) of the silicon carrier substrate. Other means to isolate the membrane exist, the most popu-

lar being the use of a sacrificial layer that is subsequently removed after the device has been fabricated [7].

The use of AlN as the piezoelectric in thin film in FBAR devices was first realised by Lakin et. al. in the early 1980's [8, 9]. Already at this time, the application was as key elements in signal filters in the UHF and microwave frequency range. The switch made from ZnO to AlN as the piezoelectric film was due to its superior mechanical and electrical properties. In addition, AlN is IC compatible.

For commercially available devices, the FBAR is currently the dominating design featuring Q factors around 2000 and high coupling factors with high reproducibility. These FBARs constitute the frequency selective units in the RF front-end of mobile hand-sets. The electrode material in FBAR is Mo due to its high acoustic impedance, low resistivity, and relatively high sustainability to electromigration with a power handling capability of around +30 dBm.

In Paper IV, the use of NiSi as an alternative to Mo electrodes was investigated. The motivation of using a silicide over a pure metal is the potential use of FBAR devices in high power applications (> 30 dBm) and high temperature sensors. A number of silicides are currently used within IC fabrication, of which NiSi is the most versatile for FBAR applications due to its low resistivity, low formation temperature, and minimum silicon consumption. However, the use of silicides as FBAR electrodes, requires the fabrication of NiSi with a thickness on the order of hundreds of nanometers, which from a fabrication point of view, is a rather extreme requirement.

In this work, a unique process for the fabrication of arbitrarily thick NiSi has been developed. The process relies on the deposition of a multilayered Ni and Si composite structure that during the anneal step form a smooth ($R_a \sim 1$ nm) and low-resistive phase nickel silicide. It was found that the NiSi surface was not suitable for direct AlN growth. Thus, a Ti seed layer was deposited to provide a better crystallographic match to AlN. It was found that, the performance of FBAR devices with NiSi electrodes was comparable to those with Mo electrodes with one exception. Due to the higher resistivity NiSi, the Mo device had a higher series Q factor.

2.2 Solidly mounted resonator

The second device, Fig. 2.1(b) is the Solidly Mounted Resonator (SMR), based on the theory presented by Newell in 1965 [10]. The SMR was first realised by Lakin et al. in 1995 [11] and since then a number of companies and academic institutions have focused their research on the optimisation of the design in order to reduce the mechanical losses and increase the Q factor and coupling coefficient [12, 13, 14, 15]. Some of their results are discussed in the next chapter. BAW filters based on the SMR configuration operating at 8GHz have been demonstrated [16]. Since the SMR is fabricated with one side firmly attached to the substrate, this device can only be used for resonator ap-

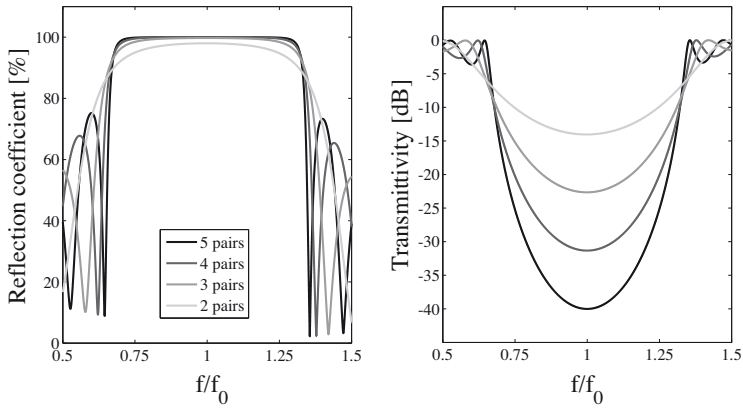

Figure 2.2: Calculated reflection coefficients and transmittivities of a dielectric AlN/SiO_2 Bragg reflector with increasing number of reflector pairs. At least five pairs are required for sufficient reflection.

plications if an adequate acoustic isolation can be provided between the two. This is done using an acoustic mirror, or Bragg reflector.

2.2.1 The Bragg reflector

The SMR represents a more robust design since it does not require the fabrication of a free-standing membrane. Instead, acoustic isolation from the substrate is provided by an acoustic mirror, also called Bragg reflector.

A Bragg reflector is a multilayered structure composed by a sequence of high and low acoustic impedance layers. The thickness of these layers are one quarter of the acoustic wavelength at resonance. The reflector works by reflecting a portion of the acoustic energy back into the resonator at each interface. The industry standard composition for Bragg reflectors are SiO_2 and W [13], since these two materials present the largest impedance ratio Z_H/Z_L readily available in micro-fabrication tools. SiO_2/W reflectors require only two pairs of layers to provide sufficient reflection. Since the metal layers in the reflector will couple capacitively to the input pads of the resonator, it is important that the reflector is patterned to prevent the parasitic capacitance from degrading the coupling coefficient of the device.

Alternatively, dielectric Bragg reflectors ca be fabricated using SiO_2 and AlN layers [12], but due to the much smaller impedance ratio of these materials, the Bragg reflector requires at least five pairs for high Q devices. In Fig. 2.2 the reflection coefficient and the transitivity of a dielectric Bragg reflector as defined in Paper VI is shown as a function of number of pairs.

Since the portion of the acoustic energy stored in the Bragg reflector are outside the electric field between the electrodes, the coupling coefficient of SMRs is lower than those of equivalent FBARs by about 1%.

Within the scope of this thesis, three different kinds of Bragg reflectors have been fabricated. The first is the SiO_2/Mo reflector which is comprised by three reflector pairs. Even though the Mo-based reflector requires an extra layer, as compared to that of W. The in-plane stress associated with the relatively thick sputter deposited W films were too large and prevented the films from adhering to the SiO_2 layer and even bending the substrate. Thus, Mo was chosen as the high impedance metal in the Bragg reflector since the film stress could be controlled.

The second reflector type is the SiO_2/AlN dielectric mirror. The advantage of this type, as was pointed out earlier, is that it does not require patterning. This type of reflector was fabricated for Paper VI and VIII where the parasitic capacitance otherwise would have degraded the performance of the devices.

The third type, featured in Paper I is the Al/Mo all-metal Bragg reflector. In the pre-study of the paper, the potential advantages of this type of mirror configuration were many, including a higher Q factor, high power handling capabilities, efficient resonator cooling, and cheap packaging to mention a few. Out of these, only the first one could be verified experimentally.

The basic idea in this paper is that a conductive Bragg reflector could replace, or rather eliminate the need for electrodes in the resonator stack. Since the electrodes take up a certain volume of the acoustic cavity, they present, from a piezoelectric point of view, "dead" regions that only for particular cases contribute to the coupling coefficient [17]. If the resonance frequency of the resonator is increased, i.e. the layers in the stack become thinner, the volume taken up by the electrodes, relative to the piezoelectric, is increased if degrading series resistance effects are to be avoided. Thus the coupling coefficient of the device is reduced. In addition, as the thickness of the AlN film is reduced, the texture of the piezoelectric film is degraded since this generally improves with thickness. Thus, the fabrication of high frequency high Q resonators is complicated.

With a conductive Bragg reflector the entire acoustic cavity is comprised by piezoelectrically active material. Thus, the coupling coefficient of the device becomes independent of frequency. In addition, even at frequencies as high as 10GHz, the total thickness of the Bragg reflector on each side of the AlN is thicker than the FBAR electrodes at 2GHz, which means that series resistance effects will not degrade the Q factor of the resonator. For a given frequency the thickness of the AlN is thicker in the proposed design compared with a conventional resonator which also should improve the Q factor of such devices.

Currently, further development of the proposed design is limited by the lack of a low impedance metal other than Al, the properties of which is not favourable for state-of-the-art resonator devices. If the conductive Bragg reflector should come to its right and provide the high Q and high power handling capabilities suggested, another low-impedance material, not as prone to electromigration as Al must be found. In light of this, the use of NiSi for electrodes and Bragg reflector applications was investigated in Paper IV.

The third type of acoustic mirror, is the dielectric SiO_2/AlN Bragg reflector used in Paper VI and VIII. As is shown in Fig. 2.2, this type of reflector requires five pairs, for a sufficiently high reflection coefficient. The many layers in the structure, put stringent requirements on the stress levels in the film in order to avoid release from the substrate and excessive substrate bending. Using a dielectric Bragg reflector, electrical losses due to capacitive coupling to the electrode pads are removed, and thus the need for reflector patterning is avoided. As such, this configuration is suitable as a low loss substrate for the MCM microwave oscilator in Paper VI and the study of Q degradation in sensor arrays in Paper VIII.

2.3 Plate wave resonators

Plate wave resonators (FPAR), as seen in Fig. 2.1 (c), have the same basic topology as that of FBARs. The major difference between the two devices is that the plate acoustic wave excited in the piezoelectric propagate parallel to the surface, thus using the plate as a waveguide. The thickness of the plate is a small fraction of the wavelength which means that only the lowest order symmetric (S_0) and anti-symmetric (A_0) is supported. Plate waves are generally dispersive meaning that the phase velocity varies with the plate thickness and wavelength ratio. In Paper II it is found that the S_0 mode exhibits low dispersion if the thickness of the plate is in the range 0.1λ to 0.3λ.

Plate waves are excited either by means of interdigital transducers (IDTs) fabricated on top of the AlN membrane, or by lateral field excitation (LFE). Using IDTs to launch and receive the acoustic wave, the electric field is parallel to the propagation direction, analogous to surface acoustic wave (SAW) devices. For some applications, this is preferred since the definition of the IDTs only require one critical lithography step. The main advantage of using IDT excited plate, or Lamb waves over SAW, is the high phase velocity in excess of 10000m/s which can only be matched by SAW devices by using special high velocity substrates as in Paper II. For LFE excited plate wave devices, the electric field is normal to the propagation direction, and a more efficient coupling between the electric and acoustic field can be achieved [18]. This is, however, at the cost of a more complicated process flow.

The high phase velocity of plate waves enables electroacoustic devices operating in the 500MHz -5GHz range using conventional low resolution lithography [19].

2.4 Simulation and modelling

Time and cost saving modelling techniques are important tools when designing electroacoustic devices. As was discussed in section 1.1, the phase velocity v_{ph} of an acoustic wave and the acoustic impedance Z, are determined by both the density and stiffness of the material. Since a resonator may consist of many different layers, with different material properties, the description of such a multilayered structure, require the use of theoretical models. Two popular one dimensional models are the Mason model [20, 21] and the Nowotny-Benes model [22, 23], respectively. Both these use an analytical approach to calculate the frequency response of the device based on the material parameters of the constituting materials, such as density, elastic constants, piezoelectric and dielectric constants. Below is a summary of the two models used within the scope of this thesis.

2.4.1 The Mason model

The Mason model is one of the most frequently used in the design of electroacoustic resonators and filters. The model uses a transmission line concept in which the piezoelectric plate is a three port network having two acoustic ports and one electric port, as illustrated in Fig. 2.3. If the boundary values of the acoustic ports are given, the impedance at the electrical port can be calculated as a function of frequency. If we consider the case of a SMR, the mechanical

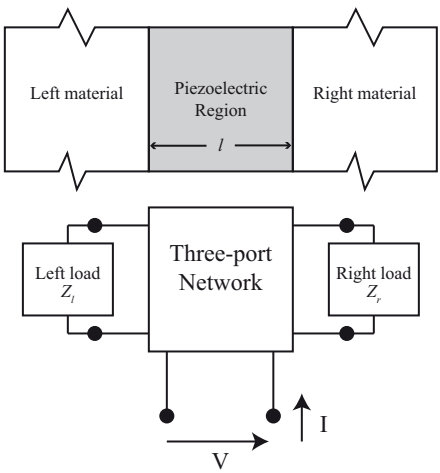

Figure 2.3: Schematic of the one-dimensional three-port Mason model. The materials on both sides of the piezoelectric plate are represented by mechanical loads Z_l and Z_r.

load on the left side Z_l represents the top electrode terminated by a mechanical short in air. On the right hand side, Z_r represents the effective mechanical impedance provided by the bottom electrode and the acoustic mirror, terminated by the characteristic impedance of the substrate. If the thickness of the

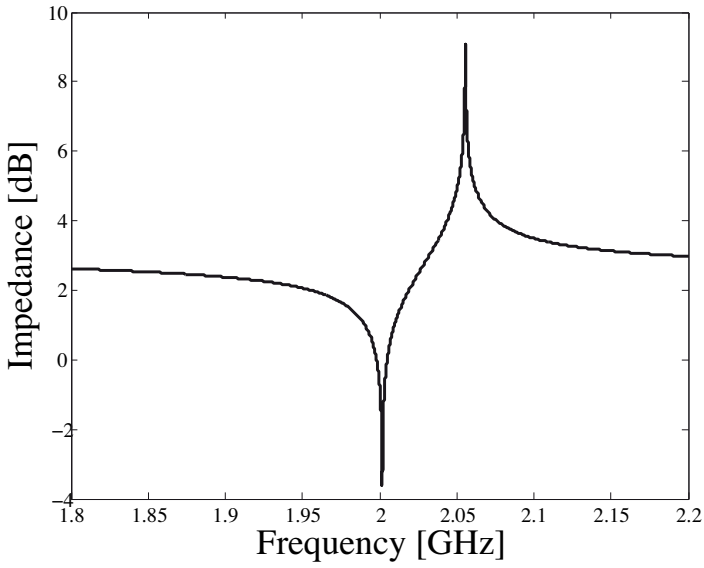

Figure 2.4: Simulated electrical impedance of a solidly mounted resonator.

piezoelectric plate is l, the phase across the plate is given by $\Phi = kl/2$, where k is the wave number. The impedance at the electrical port can then given by

$$Z_{in} = \frac{V}{I} = \frac{1}{i\omega C_0}\left(1 - k_t^2 \frac{tan\Phi}{\Phi}\right) \frac{(Z_l + Z_r)cos^2\Phi + isin2\Phi}{(Z_l + Z_r)cos^2\Phi + i(Z_l Z_r + 1)sin2\Phi}, \quad (2.1)$$

where C_0 is the static capacitance of the device, and k_t^2 as in equation 1.8. In Fig. 2.4, the calculated frequency dependent impedance of a 2GHz SMR with a c-axis oriented AlN(1720nm) film sandwiched by two Mo(172nm) electrodes is presented. The Bragg reflector consists of two pairs of SiO2(750nm)/W(615nm). In Fig. 2.5, the measured impedance response from a SMR with a five pair SiO_2/AlN Bragg reflector is shown. As can be observed in both the simulated and measured frequency responses, there are two frequencies of interest corresponding to a minimum in impedance (inhere referred to as the series resonance frequency, f_s) and an impedance maximum (inhere referred to as the parallel resonance frequency f_p.)

Acoustic transmission lines

Most of the electroacoustic devices featured in this thesis, are multilayered structures in which the acoustic wave propagates in the thickness direction. Each time the acoustic wave crosses an interface between two layers, a portion of the wave is reflected back while the other portion is transmitted. In this section we show that, by using the well known transmission line theory, the effective reflection coefficient of such a layered structure can be calculated. In this section, the mechanical loads Z_l and Z_r on the acoustic ports are calculated

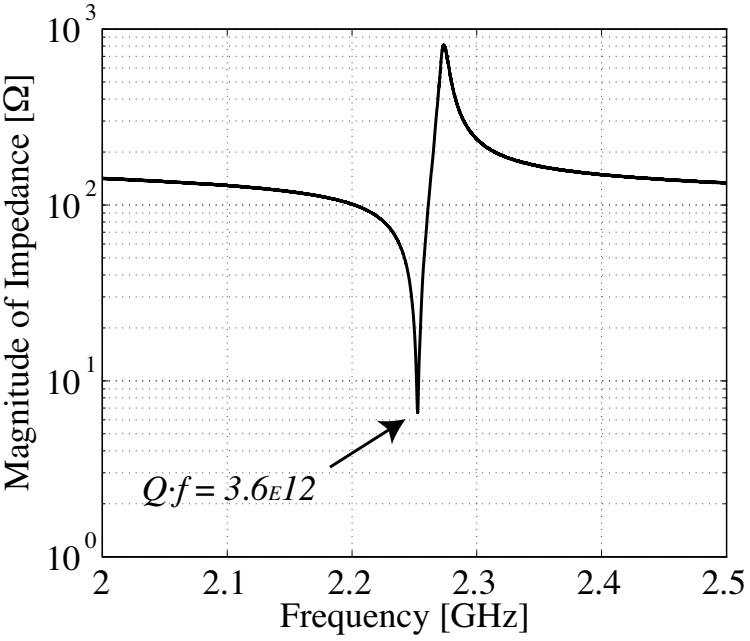

Figure 2.5: Measured impedance response of a solidly mounted resonator with a SiO_2/AlN.

as a function of frequency, using the material constants and layer thickness information.

In Fig 2.6 a multilayered structure is depicted. The structure consists of a slab of finite thickness l, sandwiched between two semi-infinite half spaces. If the characteristic impedance of the materials are z_0, z_1 and z_2, the reflection coefficient at each boundary is given by

$$\gamma_1 = \frac{z_1 - z_0}{z_1 + z_0}, \tag{2.2}$$

and

$$\gamma_2 = \frac{z_2 - z_1}{z_2 + z_1}. \tag{2.3}$$

A plane wave T_i normally incident from the left is reflected and transmitted at the first boundary $x = 0$ and then again at the second boundary $x = l$. The effective reflection coefficient for the part of the wave reflected back to the left T_r is then given by

$$\Gamma = \frac{\gamma_1 + \gamma_2 e^{-2ikl}}{1 + \gamma_1 \gamma_2 e^{-2ikl}}, \tag{2.4}$$

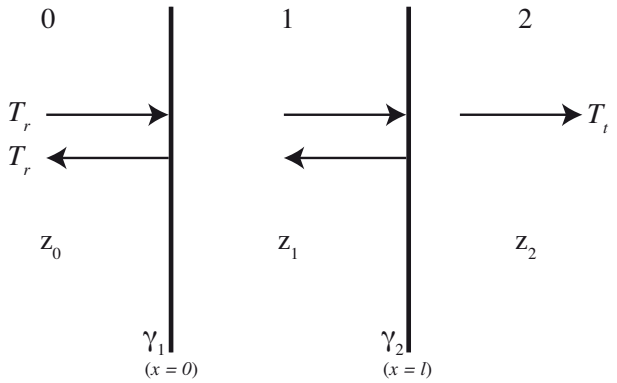

Figure 2.6: Using transmission line theory, the effective reflection coefficient of a wave normally incident on a multilayered structure can be calculated.

where k is the wave number. Similarly, the input acoustic impedance Z_{in} for the incident wave can be calculated as

$$Z_{in} = Z_0 = z_1 \frac{z_2 + iz_1 \tan kl}{z_1 + iz_2 \tan kl} \tag{2.5}$$

Since there is no wave travelling from the right, the input impedance at the second boundary can be expressed as $Z_1 = z_2$. Both equations 2.4 and 2.5 are recursive formulas and can be expressed in a more general form for an arbitrary number of layers.

$$\Gamma = \frac{\gamma_i + \Gamma_{i+1} e^{-2ik_i l_i}}{1 + \gamma_i \Gamma_{i+1} e^{-2ik_i l_i}}, \tag{2.6}$$

where the recursion is initiated on the right by $\Gamma_{i+1} = \gamma_{i+1}$.

$$Z_i = z_i \frac{Z_{i+1} + iz_i \tan k_i l_i}{z_i + iZ_{i+1} \tan k_i l_i}, \tag{2.7}$$

in which initiation is made in the same manner by setting $Z_{i+1} = z_i + 1$. The usefulness of these equations will become apparent in the chapter treating the modelling of electroacoustic devices.

2.4.2 Nowotny-Benes model

Another one-dimensional model in the Nowotny-Benes (NB) model [22, 23]. The NB model can be described as a general transfer matrix description for a one-dimensional layered structure that consists of piezoelectric and non-piezoelectric anisotropic layers. Each layer in the device structure is here represented by an 8x8 matrix containing the elastic, dielectric, and piezoelectric constants and is used to calculate the admittance at the electrical port. The

main advantage of the NB model over the Mason model is its general formulation and multi mode treatment of anisotropic materials such as AlN.

2.4.3 The Modified Butterworth-Van Dyke model

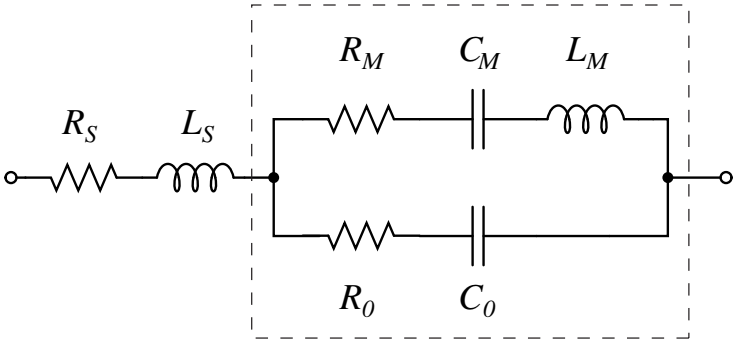

Figure 2.7: MBVD equivalent circuit model of a resonator including electric and dielectric material losses.

The Modified Butterworth van Dyke (BVD) model [24] is based on the electrical equivalent circuit in Fig. 2.7. The model is particularly useful for the evaluation of resonator performance, and extraction of device properties from electrical measurements. The model only gives accurate results close to resonance. In the model, R_S, L_S represent the metal line from the contact probe to the actual resonator and is thus used to extract contact electrical losses from the measurement data. The resonator is represented by a static arm and a motional arm. In the static arm, C_0 is the parallel plate capacitance formed by the electroded dielectric. R_0 is used to model the dielectric losses in the material. The motional arm represents the electroacoustic properties of the piezoelectric by the motional inductance L_M, motional capacitance C_M, and motional resistance R_M. Here R_M represents the acoustic attenuation in the device.

At series resonance, corresponding to a minimum in the input impedance, the electric and acoustic fields oscillate in phase, and the device is short circuited. At this frequency the current flows through the motional arm and f_s is given by

$$f_s = \frac{1}{2\pi} \frac{1}{\sqrt{L_M C_M}}. \tag{2.8}$$

At the parallel resonance frequency, the fields are 180° out of phase corresponding to a maximum in input impedance and f_p is given by

$$f_p = \frac{1}{2\pi} \sqrt{\frac{C_0 + C_M}{C_0 L_M C_M}}. \tag{2.9}$$

3. Fabrication and characterisation of Thin film BAW devices

In this chapter, the fabrication of thin film bulk acoustic wave devices is reviewed. Since the thin film piezoelectric material treated in this thesis is aluminumnitride, it is given more attention than other materials. First, a brief process flow is described, then the details of synthesis and patterning of AlN is treated, followed by material characterisation. Then the modelling of thin film resonators is presented and finally, the device characterisation is discussed.

3.1 Device fabrication

3.1.1 SMR process flow

In this section a brief description of a resonator process flow is given. The SMR is considered but the most of the processes are shared with the other types of resonators.

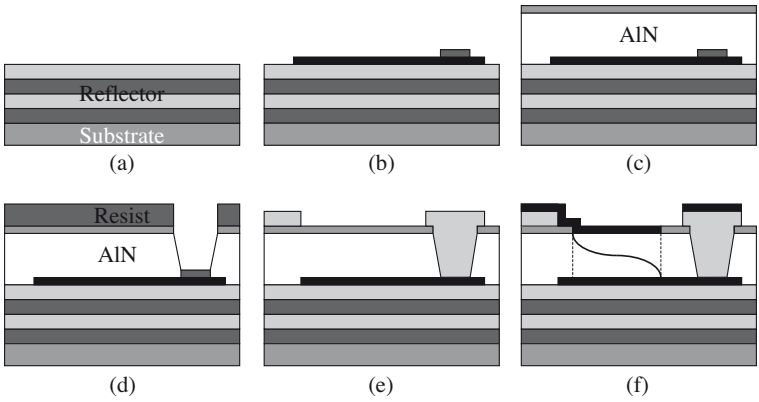

Figure 3.1: Schematic process flow for a BAW SMR. (a) Bragg reflector deposition, (b) Bottom electrode and etch stop definition, (c) AlN deposition (with a protective SiO_2 layer), (d) AlN via hole etching using photoresist hard mask, (e) Pad metallisation, and (f) Top electrode definition.

In Fig. 3.1, the general outline of the process steps are shown schematically. First, for SMR fabrication, the Bragg reflector is deposited on a cleaned Si substrate, by sputtering, Fig. 3.1(a). Depending on the composition of the reflector, the number of layers deposited may vary. The top layer in the reflec-

tor is has a low acoustic impedance and is typically SiO_2. Then the bottom electrode is deposited by sputtering and patterned by photolithography. The same procedure is done for the etch stop, Fig. 3.1(b). In the next step, the piezoelectric AlN film is deposited by reactive sputtering, Fig. 3.1(c). On top of the AlN film a passivation SiO_2 layer is then deposited by either reactive sputtering or PECVD. This oxide is not required for the actual operation of the device, but protects the AlN surface from the subsequent process steps. As such, it adds flexibility to the process flow. Furthermore, cracks in the AlN film can appear at the topography formed by the bottom electrode and etch stop. This crack may short circuit the device so a protective oxide conveniently prevents this from happening. In the next steps, the AlN via hole is etched, Fig. 3.1(d) and the pad metallisation is deposited, Fig. 3.1(e). In the last step, the SiO_2 is patterned and the top electrode is sputter deposited and patterned, Fig. 3.1(f). The SMR is now ready for electrical characterisation.

3.1.2 Reactively sputtered AlN thin films

Reactive sputter deposition of AlN thin films has been an area of intense research over the last thirty years [25, 26, 27]. The objective has always been to understand and control the growth characteristics of these films, since the performance of the end product, i.e. the resonator or filter, is highly dependent on the quality of the piezoelectric film. From the massive amount of papers, published on this issue, the conclusion is that the proper process parameters are strongly dependent on the type of system used. At Uppsala University, the research efforts focusing on AlN deposition have so far, resulted in three theses where the optimal growth conditions for our system have been defined [28, 29, 30]. Their findings are summarised in the following two sections.

Synthesis of c-axis oriented AlN film

In our sputter system (Von Ardenne CS730), synthesis of c-axis oriented AlN is done with pulsed DC reactive magnetron sputtering. The system has two process chambers that fits four magnetrons and four substrate holders, each. The holders are loaded from a small load-lock and a transfer chamber, common for both process chambers. The entire unit is controlled via a computer interface with a script running to control the deposition. Each chamber is evacuated with a 800l/s turbo-pump. The AlN chamber is equipped with an additional Ti-sublimation pump in the AlN chamber to getter O_2 and further reduce the base pressure. Furthermore, the targets mounted in the AlN chamber are Al, Mo, Ti, and W, all of which getter oxygen. This means that on a good day, oxygen levels in the AlN film are below 0.5%.

The AlN films in this thesis, were deposited from a 150 mm 99.999% pure Al target under a balanced magnetron. The process gases used were Ar and N_2, the ratio of which has been varied to compensate for the in-plane stress of the AlN. The total flow was always 60 sccm. Before the deposition process begins, the system is pumped for two hours to reduce the base pressure down $< 5 \cdot 10^{-8}$Torr. Then the target surface was cleaned with an Ar discharge to

Table 3.1: *AlN Deposition parameters for c-axis orientated AlN*

Target	Al (99.999%)
Substrate to target distance	55 mm
Base pressure	$< 5 \cdot 10^{-8}$Torr
Process pressure	$2 \cdot 10^{-3}$Torr
DC discharge power	900 - 1200W
Ar gas flow rate	15 - 20 sccm
N_2 gas flow rate	40 - 45 sccm
Deposition rate	$\sim$1 nm/s

remove any oxide layers that may have formed on the target since the last deposition. During this time a shutter covers the substrate. For AlN deposition, the applied power of the DC discharge have been varied between 900W to 1200W. A summary of the process parameters are presented in Table 3.1.

Synthesis of c-axis inclined AlN film

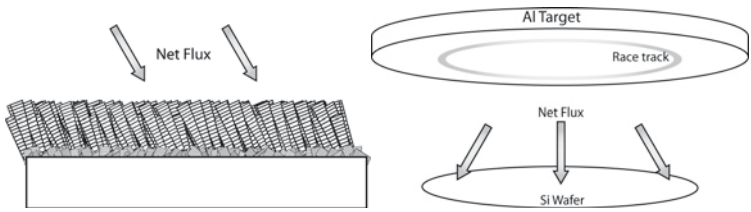

Figure 3.2: Illustration of the deposition of c-axis tilted AlN (a). First a thin seed layer with a large population of (103) oriented grains is deposited. Then the pressure is reduced to promote competitive growth of (002) grains. In (b), the mean direction of the net flux of sputter species recieved at the substrate surface at low pressure.

The fabrication thin film resonators operating in the thickness shear mode, requires that the c-axis is tilted, or inclined from the substrate normal. A controlled fabrication process of such films is of great interest for sensor applications since it allows the resonator to operate in liquid environments. The deposition process of AlN films with a mean tilt of the c-axis, developed at Uppsala University is a two stage process [31], as illustrated in Fig. 3.2(a). During the first stage, a special seed layer is deposited which subsequently promotes a tilted grain growth. This is done by depositing a very thin AlN film at a relatively high pressure of 20 mTorr or more precisely in the diffusion limited regime. The seed layer contains a large population of (103) oriented grains, and is on the order of 100 nm thick. In the second stage, the process pressure is reduced to 2 mTorr. The mean free path of the atomic flux

is now larger than the substrate-to-target distance and the deposition continues in the competitive growth regime. Since the net deposition flux incident on the substrate is not normal to the substrate surface, as indicated in Fig. 3.2(b), the AlN film will now grow along the c-axis planes of the (103) grains that are oriented toward the mean atomic flux on the substrate.

3.1.3 AlN etching

Selective etching of AlN thin films is of great importance as it is a requirement for the fabrication of contact via holes to the bottom electrode. For IC integration using the Above-IC technology, AlN etching is needed for the removal of the sacrificial layer and subsequent membrane release [32]. Among the III-IV materials, AlN has the highest bond energy of 11.52 eV/atom which makes it difficult to remove without subjecting it to a quite harsh treatment. A successful process must therefore take into consideration the macroscopic effects of the etch. Choosing the proper etch stop and etch mask is thus of outmost importance. In this thesis, both dry and wet etch processes have been explored.

Dry etching

Dry etching of AlN with an acceptable etch rate around 100 nm/min, can be accomplished in a high density plasma system such as an inductively coupled plasma (ICP) reactor using Ar, Cl_2 and BCl_3 chemistry [33]. In a recent survey, Engelmark et. al. [34] found the etch process to be a combination of physical etching caused by ion bombardment to break the Al-N bond, and chemical etching with the formation of gas-phase Al_2Cl_6 and N_2. Furthermore, the etch rate was highly dependent on the bias voltage applied to the substrate during etching. The etch rate of AlN as a function of the applied RIE power is shown in Fig. 3.3. In view of this, the appropriate etch mask and etch stop material must be able to withstand both the ion bombardment and the chemical reactions from the etch species with sufficient selectivity. In our experiments, a Ni hard mask was first chosen as the etch mask and etch stop, owing to its high selectivity to the Cl based etch chemistry. The Ni etch stop was deposited by sputter deposition and lift-off lithography. Similarly, the Ni hard mask was deposited onto the AlN surface and then etched with 100% HNO_3. As masking material for this etch, Al was used.

Although Ni is an appropriate mask for AlN etching, the process involves quite a large number of time consuming steps, and the repeated treatment of very hazardous acids. Since the Ni mask needs to be removed after etching, the wafer is immersed in 100% HNO_3 which also attacks the etch stop. Since the nitric acid is a highly oxidising acid, the only electrode material that will survive this process is Al. Using Al as the electrode material may be acceptable for experimental devices, but for real devices, it does not provide provide a high enough coupling coefficient, nor does it withstand high RF power levels.

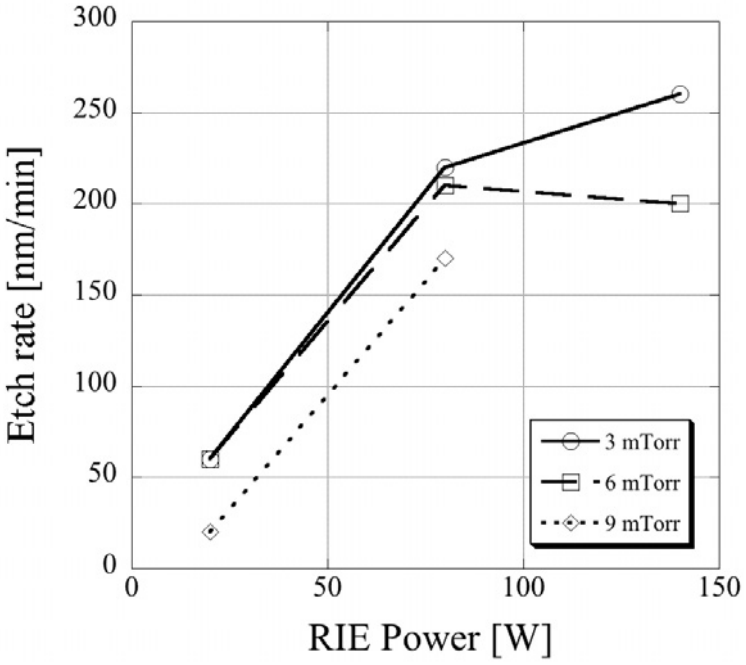

Figure 3.3: Etch rate of AlN film as a function of applied RIE power. The applied bias in in the range of 50 to 300V.

To address these critical points, a 10μm thick layer of AZ 4562 photoresist, was chosen as the etch mask. The resist was spin deposited onto the substrate and patterned using conventional photolithography. Since the etch mask in this case, is consumed by the ion bombardment during etching, perfectly anisotropic side-walls are not achievable here. In Fig. 3.4(a) the regression of the photoresist, resulting in a tapered etch slope can be observed. After the etch process, the resist was easily removed by immersion in an acetone ultrasonic bath. It is noted here, that Ni may still be used as an etch stop during the AlN etch, but if another metal than Al is used as bottom electrode, it may not be possible to remove it afterwards. The above described process featuring AZ4562 and 20W of RIE power was used as the etch mask material in Papers I, III, V, VII, VIII.

Wet etching

Wet etching of AlN is of great importance since it comes with a considerable cut in production cost. Moreover, if the etchant has a high enough selectivity between the AlN and the bottom electrode, the etch stop can be left out of the process flow. Some of the wet etchants reported in literature, and those used in this work, are listed in Table 3.2. It is noted that the etch rate of AlN is dependent not only on the temperature, but also on the crystal quality of the deposited film [35]. In Paper IV, the AlN is etched using Tetramethylammo-

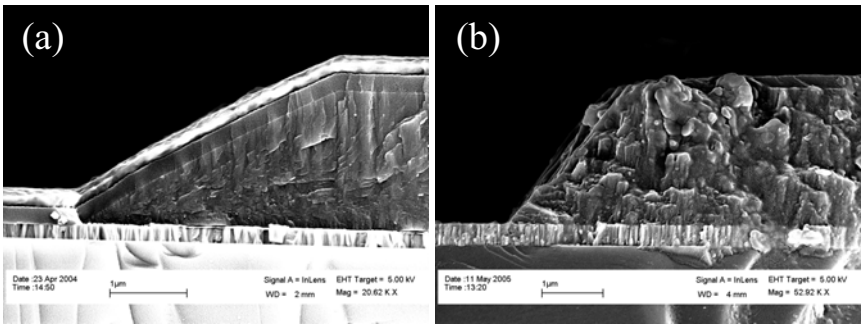

Figure 3.4: SEM micrographs of AlN etch profiles. (a) Dry etching of AlN using AZ4652 photoresist as masking material. The tapered etch profile is caused by the consumption of the mask. After etching the wafer has been processed to illustrate the prospects of using this method. (b) Wet etching of AlN using TMAH solution. SiO_2 was used as etch mask, and Mo bottom electrode as etch stop.

Table 3.2: *AlN wet etchants*

Etchant	Temperature [°C]	Rate [nm/min]	Ref
Sodium Hydroxide	75	50	[36]
Potassium hydroxide	25	2265	[36]
AZ400K photoresist developer	25	∼6-1000	[36]
TMAH 25wt%	25	∼60	This work

nium hydroxide (TMAH) 25 wt.%. TMAH is a strong base that is normally used for anisotropic etching of Si above 70°C. At room temperature, no etching of Si or SiO_2 has been observed. In our process, the AlN surface is passivated with a PECVD SiO_2 layer to serve as an etch mask. The SiO_2 is then patterned and etched with buffered HF solution. During the etch process, the wafer is immersed in TMAH with mild stirring. In Fig. 3.4(b), the result of the etch process can be seen. In this case Mo was used as bottom electrode. In Paper IV, both Mo and NiSi showed no sign of deterioration to the TMAH etch process at room temperature.

It is pointed out here that TMAH is not a suitable etchant for c-axis tilted AlN films. Etching of such films will result in substantial undercut of the mask. It is likely that the etch is faster along the grain boundaries due to weakened bonds [35]. This fact supports the anisotropic profile shown in Fig 3.4(b) and would for tilted grains, increase the lateral etch rate.

3.1.4 AlN characterisation

The characterisation of AlN in terms of composition, film texture, and piezoelectric properties is crucial in the fabrication of electroacoustic devices.

AlN texture

One of the most common methods for characterising the texture of AlN is by X-ray Diffraction (XRD) measurements. The measurement data give valuable information on the degree of orientation of the deposited film. Generally, two measurements are required. The first, known as the Θ-2Θ scan. Crystal planes parallel to the substrate surface give rise to strong reflections. For AlN the desired peak, representing the (002)-plane, is found at around 36°. In the second scan, known as the ω-scan or rocking curve, the X-ray source and detector is locked on the (002)-peak and the substrate is "rocked" in the ω co-ordinate. The degree of texture of the AlN film is determined by the full width at half maximum (FWHM) of the rocking curve.

Thickness measurements

The fabrication of electroacoustic devices requires very good thickness control. For SMRs the acoustic cavity is matched to the Bragg reflector to prevent acoustic leakage to the substrate. For Lamb devices, the dispersion relation is determined by the film thickness to wavelength ratio. In this thesis, the thickness of deposited AlN films was determined by laser interferometry. This is a non-contact method with a resolution below 1 nm. Typically, the variation in thickness along the radius of a 100 mm wafer for a 2μm thick AlN film, fabricated in our system is 10%.

Film stress measurements

The control of the in-plane stress in AlN is very important when fabricating resonators of membrane type. If not controlled, the film stress can easily become large enough to cause a deformation of the membrane and even the substrate. The stress in the film is determined from the substrate radius of curvature before and after film deposition. A laser beam is reflected from the substrate surface into a photo detector. The measurement is performed while the beam scans over a distance along the diameter of the wafer. Compressive stress produces a convex curvature of the substrate and is denoted by negative stress values, whereas tensile stress causes the substrate to bend with a concave curvature and is denoted by positive values. In Fig. 3.5 the in-plane stress of a 2μm AlN film as a function of the Ar/N_2 flow ratio is shown.

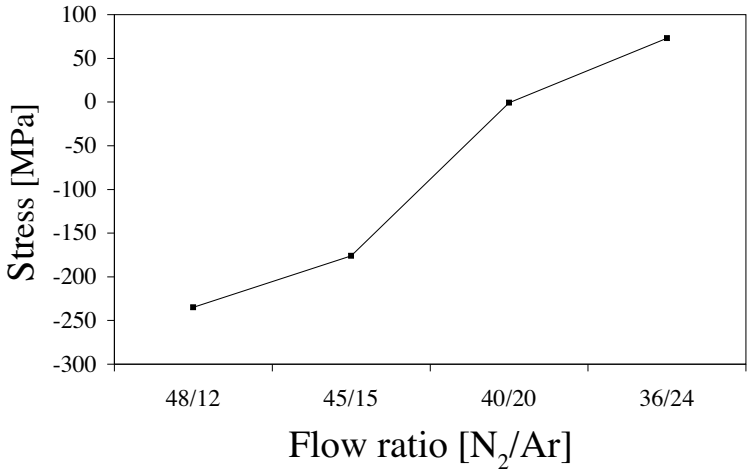

Figure 3.5: AlN in-plane stress vs. Ar/N_2 flow ratio. The line connecting the points is guidance to the eye.

3.2 Electric characterisation

3.2.1 S-parameter measurement

Scattering parameters or S-parameters [37], are used to describe the small signal electrical behaviour of linear electrical networks terminated by matched loads. The term "Scattering" refers to the quantification of the reflected and transmitted parts of the signal when incident on an impedance discontinuity. Mathematically, S-parameters can be described using transmission line theory and and matrix algebra. For a two-port network, the S-parameter matrix is given by:

$$\begin{pmatrix} b_1 \\ b_2 \end{pmatrix} = \begin{pmatrix} S_{11} & S_{12} \\ S_{21} & S_{22} \end{pmatrix} \begin{pmatrix} a_1 \\ a_2 \end{pmatrix}, \tag{3.1}$$

where a_1 and a_2 are power waves incident on port 1 and 2, respectively. b_1 and b_2 are the exiting waves from port 1 and 2, respectively. Using the maximum power transfer theorem and the fact that both ports are terminated by matched loads, all four S-parameters can be calculated.

If the measured network only has one port, the impedance and admittance of this network is given by:

$$Z_{11} = Z_0 \frac{1+S_{11}}{1-S_{11}} \quad and \quad Y_{11} = \frac{1}{Z_0} \frac{1-S_{11}}{1+S_{11}}, \tag{3.2}$$

where Z_0 (usually 50Ω) is the characteristic electric impedance, or matched load of the system.

In this work, the S-parameters of the resonators have been measured with a two-port vector network analyser (VNA) that measures both the amplitude and the phase of the scattered signal. The ports of the VNA are connected to the device using cables and probes capable of conducting on-wafer measurements as shown in Fig. 3.6. Inside the dashed box, a schematic of the probe tip configuration is shown. The pitch of the ground-source-ground (GSG) tips is 150 μm. The VNA is set-up by adjusting the power level and frequency sweep. Since the cables connected to ports are outside the calibration reference of the VNA, a short-open-load-through (SOLT) calibration step is performed with a specific calibration substrate. This moves the network frame of reference to the tip of the probes. This basic system set-up can be extended to perform temperature characterisation by placing the DUT on a heated chuck. Furthermore, to analyse the frequency response as a function of an electric field, the signal probe tip can be biased between -40V - +40V DC by connecting an external voltage source to the VNA.

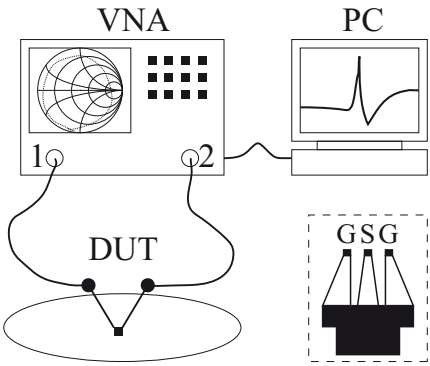

Figure 3.6: Schematic of 2-port measurement set-up on-wafer using GSG probes.

3.2.2 Device parameter extraction

As indicated in Fig. 3.6, the VNA system is connected to a computer, via a GPIB interface, to which the measurement data can be recorded. This data is subsequently analysed with Agilent Advanced Design System (ADS) software, where the MVBD parameter extraction is done. The extraction routine is based on error minimisation and least-squares fit between the measurement data and the MBVD equivalent circuit. In Fig. 3.7 the measured admittance Y_{11}, and fitted parameters, of a one-port SMR sensor in liquid is shown.

The quality factor

The quality factor (Q), is indicative of the rate at which energy is being dissipated in the electroacoustic device. In the resonator, the energy oscillates between kinetic and potential forms, and during these cycles, some energy is

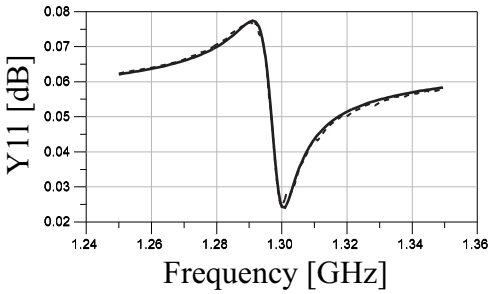

Figure 3.7: Admittance fit of a inverted SMR sensor in liquid environment from Paper VIII

inevitably wasted due to internal friction and other loss mechanisms. For a mechanical resonator, the general definition of the quality factor is

$$Q = 2\pi \frac{\textit{Energy stored}}{\textit{Average energy dissipated per cycle}}. \tag{3.3}$$

Consequently, a high Q is one of the most desired parameters in electroacoustic device design as it indicates a low rate of energy dissipation. In filter design, a high Q is required to reduce the insertion loss and provide a steep skirt roll-off. For oscillators, a high Q reduces the phase noise, improves the frequency stability, and reduces the start-up time. A high frequency stability is furthermore beneficial for high resolution sensors.

To find the Q factor of thin film resonators, a number of methods exist. One of the most reliable methods of Q extraction is related to the impedance/admittance phase slope. The Q factor is then given by

$$Q_{s,p} = \frac{f_{s,p}}{2} \left| \frac{\partial \phi_{Y,Z}}{\partial f} \right| \tag{3.4}$$

However, if the resonator has a lot of spurious modes near the resonance frequencies, this method cannot be used directly. Then a model fit according to the MVBD model must first be conducted [38].

Another practical direct extraction method is to determine the bandwidth Δf at the -3dB level of the admittance and impedance curves according to

$$Q = f/\Delta f_{-3dB}. \tag{3.5}$$

The energy losses within and in the vicinity of the resonance cavity can be divided into two major mechanisms: electrical and mechanical. From the electrical point of view, these are quite easily characterised by resistive losses in the electrodes, contact pads and transmission lines leading to the active area of the resonator. These losses are more prominent at the series resonance f_s since, at this frequency the resonator is short circuited.

The mechanical losses are slightly more complicated, but can be further divided into two possible mechanisms [38, 39]: mechanical losses in the different materials (associated with a poorly textured AlN film, or low Q materials in the electrodes/Bragg reflector), and laterally escaping waves (due to coupled Rayleigh-Lamb modes). To reduce the effects on Q of the former mechanism, optimisation of process parameters is required. The recipe for the cancellation of the latter mechanism has recently been presented, in which a raised or recessed border frame is fabricated on the top electrode [14, 15].

These two mechanisms are associated with both FBAR and SMR. However, in the SMR case, the list of loss mechanism becomes longer. While the $\lambda/4$ Bragg reflector is optimised to reflect longitudinal waves, the transmission of wave with shear polarisation is very high. Shear waves can for example be excited if the AlN film is poorly textured. By tuning the Bragg reflector out of the $\lambda/4$ condition, the reflector can be designed to reflect both longitudinal and shear waves [13]. Simulated transmittivities of this phenomenon can is illustrated in Fig. 3.8.

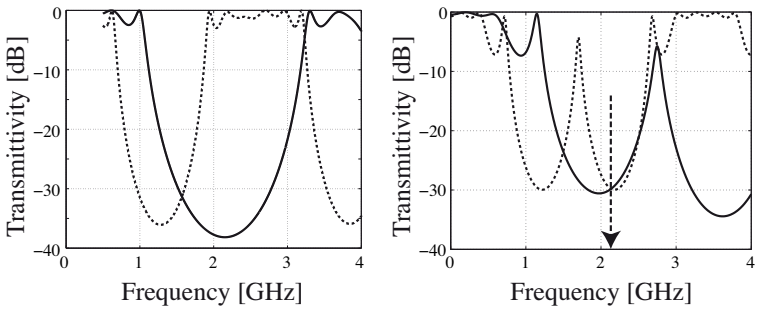

Figure 3.8: Simulated transmittivity for longitudinal (solid line) and shear (dashed line) acoustic waves. For the $\lambda/4$ Bragg reflector (left) shear waves are not reflected at the fundamental resonance. An optimised reflector (right) can reflect both modes at the expense of reduced coupling. The arrow indicates the desired resonance frequency.

The Coupling coefficient

The second important device parameter is the effective electromechanical coupling coefficient k^2_{eff} and is a measure of how efficiently the device converts electrical energy to mechanical energy, and vice versa [38]. The electromechanical coupling coefficient k^2_t is defined for a piezoelectric film by Eqn. 1.8. Since the acoustic cavity of a composite resonator contains non-piezoelectric materials, i.e. the electrodes, k^2_{eff} will differ from, and in some circumstances be even larger than, k^2_t. This is due to an improved match between the acoustic standing wave and the linear electric field in the piezoelectric [17]. Moreover, if the acoustic impedance of the electrodes is higher than that of the AlN film, a improved reflection coefficient is obtained.

For a high Q resonator, the coupling coefficient is approximately given by [3]

$$k_{eff}^2 = \frac{\pi^2}{4}\frac{f_p - f_s}{f_p}, \tag{3.6}$$

where f_s and f_p is the series and parallel resonance frequencies respectively.

The factors directly influencing k_{eff}^2 are associated with electroacoustic energy conversion. If the AlN film for example is poorly textured or has flipped grains [40] the actuation will be counteracted. To address this issue, proper choice of bottom electrode with appropriate texture and smoothness [41] is required. For SMR with metal in the Bragg reflector, a parasitic capacitive coupling with the contact pads will reduce the coupling coefficient further. This parasitic coupling can only be eliminated by patterning of the Bragg reflector as seen in Fig. 3.9, or by fabricating the SMR on a dielectric reflector.

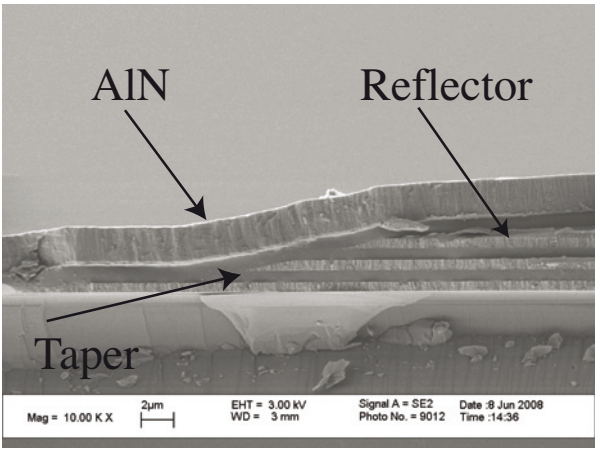

Figure 3.9: Patterning of the Mo metal layers in the Bragg reflector.

Electric field coefficient of frequency (ECF)

In Paper III, the electric field sensitivities of FBAR, SMR, and FPAR devices were measured by applying a DC bias to the signal probe as indicated in Fig. 3.10. While stepping the magnitude and polarity of the applied field, a linear shift in the resonance frequency could be observed. The observed shift is a combined effect of the inverse piezoelectric effect where the volume and density of the piezoelectric material change, and the elasto-electric effect in which the phase velocity in the piezoelectric varies due to a softening or stiffening of the elastic constants. In the comparative study of the electric field sensitivity of the BAW resonators illustrated in Fig. 2.1, it was found that for the longitudinal mode, the FBAR exhibits the largest sensitivity with an ECF of 20.2 ppm/MV/m. This can be compared to an ECF of 12.0 ppm/MV/m for

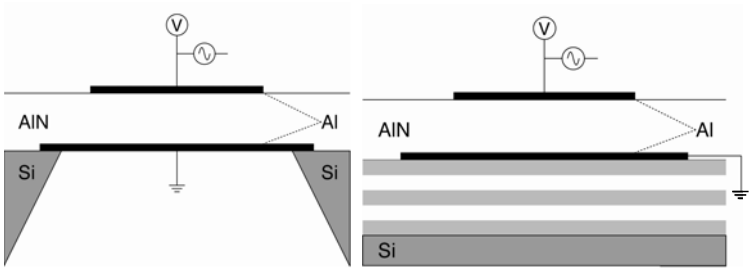

Figure 3.10: Schematic of FBAR and SMR devices with a DC bias connected to the top (signal) electrode. the set-up is used to determine the electric field coefficient of frequency (ECF) of each device.

the SMR and 7 ppm/MV/m for the FPAR with biased reflectors. The most important results of the study was the negative ECFs achieved for shear mode operation.

3.2.3 Powerhandling capabilities

The threshold power handling capabilities of BAW FBAR and SMR duplexers are reported in the literature to be around +30 dBm without any sign of irreversible damage [42, 43]. Given the small insertion loss of the resonators, this corresponds to a power density on the order of $\sim$1 MW/cm^3. The main failure mechanism is not limited by the piezoelectric film, but rather the degradation of the Mo electrodes due to electromigration. To measure the power handling capabilities of the fabricated SMR structures from Paper I and Paper VI, a separate measurement system was devised. The set-up is pictured in Fig. 3.11. In this set up, a signal generator (1) is connected to two power amplifiers with +30dB (2) and +10 dB (3) amplification, respectively. To protect the amplifiers from reflected power waves, a circulator (4) was also connected. The

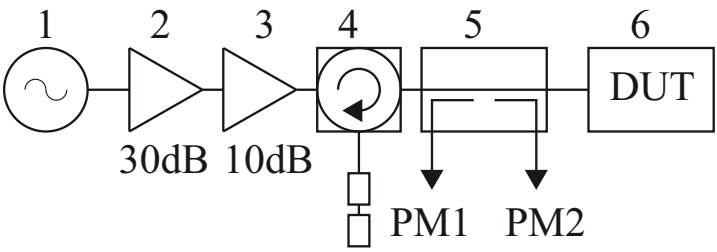

Figure 3.11: Power measurement set-up. First comes the signal generator (1) followed by two power amplifiers (2)(3). A circulator (4) protects the amplifier from reflected power. Next, a directional coupler (5) sends the incoming and reflected signal to their respective power meters. Power dissipation in the DUT is determined.

circulator will send any reflected power down into an attenuator. Next is the directional coupler (5) with which the incoming and reflected power can be measured. To the test ports of the directional coupler two power meters were then connected in order to measure the power dissipation in the DUT (6). The first power meter measures the input power, and the second the reflected. The difference between input and reflected power is dissipated in the SMR.

First, the local minimum in the S_{11} parameter, was localised with the VNA set-up of Fig. 3.6. This is then set as the output frequency of the signal generator. As the power is increased, the frequency shift in the SMR due to temperature drift, the output frequency of the generator is adjusted to the new minimum. The electrode material in both type of resonators, is Al which is less temperature stable, and more prone to electromigration, than Mo. Irreversible degradation of the resonators occurred already at +23 dBm. In Fig. 3.12, SEM images from a 200 nm Al top electrode before and after power measurements is shown. After only 30 minutes the measured Q factor dropped down to 450 from 1100.

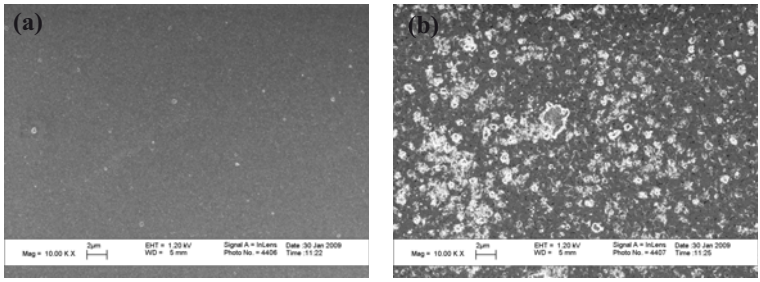

Figure 3.12: SEM micrographs of the top Al electrode of a SMR resonator before (a) and after (b) power measurements at +23 dBm. Strong indication of electro-migration can be seen.

4. Integrated BAW applications

In this chapter, applications of integrated BAW devices are described. First the hybrid and monolithic integration of the SMR with integrated circuitry in relation to Paper V and VI is discussed. Then the use of SMR integrated with a microfluidic system as described in Paper VII and VIII are considered.

Integration concepts

The prospects of integrating BAW resonators with IC technology have been one of the main driving forces behind the recent development in the electro-acoustic field. The possibility to monolithically integrate BAW devices is granted by the fact that they are fabricated using the same planar technology as ICs and materials compatible with existing process equipment. Integration results in enhancing circuit performance and decreasing cost by reducing the number of solder joints, bumps, or bond wires, and reducing the chip size for additional hand-set functionality.

Essentially, two different concepts have been developed: monolithic and hybrid integration. In monolithic integration the BAW device and the IC are fabricated, as the name suggests, on the same substrate. Depending on the order of the process flow, the integration can be either pre-, intermediate- or post-CMOS processing. Since the metal lines used for electrodes in the BAW device are not compatible with high temperatures, post-CMOS integration is most common [44, 32].

However, despite the elegance of monolithic integration, it seems that hybrid integration is the more popular and cost efficient way to go. Using hybrid integration concepts allows the use of heterogeneous substrates, which means that substrate losses, particularly in the RF frequency range can be minimised by the use of high resistive rather than low resistive silicon [45]. Hybrid, or multi-chip-module (MCM) integration is thus the concept adopted in this thesis. A conceptual drawing of the MCM concept is shown in Fig 4.1.

4.1 RF Oscillators

Wireless applications require the use of oscillators operating in the RF and microwave frequency ranges. The purpose of the oscillator is to provide a signal reference source used for time keeping, frequency conversion and carrier generation in the RF front-end of mobile handsets. Oscillators of this kind consist of an active device, e.g. a transistor, and a passive device e.g. a resonator. These two devices work in conjunction to provide the necessary conditions

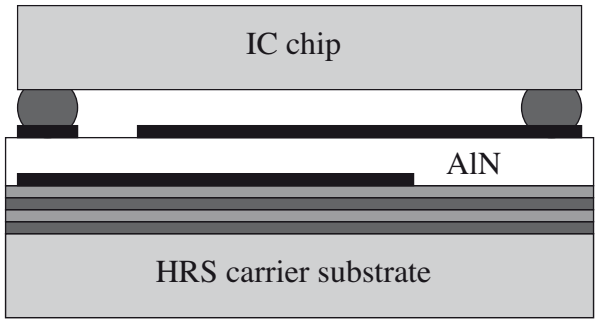

Figure 4.1: MCM integration concept. Microwave losses are minimised by using a high resistive silicon substrate for the BAW device.

for oscillations in a network to exist. To date, RF oscillators featuring co-integrated AlN based BAW resonators have been realised using monolithic, Above-IC, and MCM concepts [46, 44, 47, 48].

There are two basic types of oscillators, feedback oscillators and reflection oscillators. In this text, reflection oscillators are considered. Reflection type oscillators rely on negative resistance in the active device. A simple schematic is depicted in Fig. 4.2.

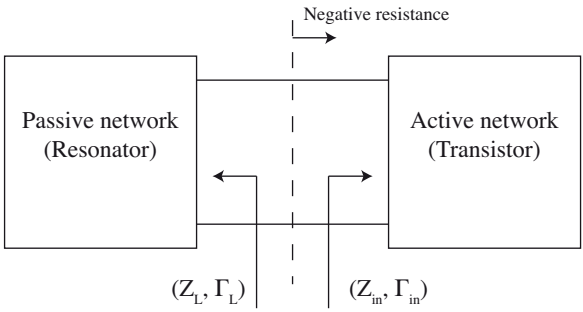

Figure 4.2: Negative resistance oscillator network

The principle of negative resistance oscillator can, in short, be described as follows[49]: For the active device, the input impedance is given by $Z_{in} = R_{in} + iX_{in}$. The passive load defined by the resonator is similarly given by $Z_L = R_L + iX_L$. Kirchoff's voltage law then yields $(Z_L + Z_{in})I = 0$. If the network oscillates, the current I is non-zero which means that $R_L(\omega) + R_{in}(I,\omega) = 0$ and $X_L(\omega) + X_{in}(I,\omega) = 0$. Since the load is passive, $R_L > 0$ and $R_{in} < 0$. The frequency of oscillation is determined by the reactance relation above.

Negative resistance at the input of the active device is created by biasing the transistor to a potentially unstable region. Then oscillations are initiated by transient or thermal noise in the network. As the amplitude increases, so does the current in the network until $Z_L = -Z_{in}$ at the designated frequency

of operation. In summary, the frequency of oscillation is determined as the frequency at which the resultant reactive component of the input impedance is zero, provided that sufficient negative resistance exists at this frequency [50]

To provide a stable output frequency, any perturbation in the current or frequency must be efficiently damped out so that the oscillator may return to its original state. This means $\partial(X_L + X_{in})/\partial\omega \gg 0$, a relation that is provided by the high Q of the resonator load. The fluctuations in the output frequency, are usually referred to as phase noise. Phase noise is defined as the ratio of power in one phase modulation sideband to the total signal power per unit bandwidth at a particular frequency offset from the output signal frequency [49, 51].

The oscillator circuits considered in this thesis are based on a common base topology. A bipolar junction transistor (BJT) is used as the active non-linear device and a high Q SMR as the passive frequency determining element. The resonator is the core component of the oscillator, in that it is the frequency selective component and its Q is the dominating factor for the phase noise performance of the oscillator. A combination of gain and feedback via the internal capacitances of the BJT, renders a negative input resistance at the emitter. A picture of the fabricated oscillator and circuit schematic is shown in Fig. 4.3.

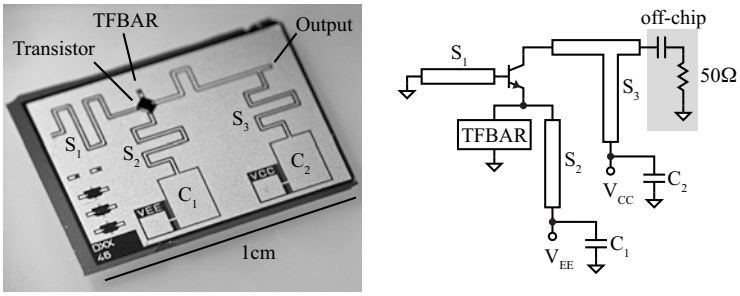

(a) (b)

Figure 4.3: (a)Photograph of the fabricated oscillator chip. (b) Schematic of the oscillator circuit.

4.2 Thin film BAW Sensors

Thin film bulk acoustic wave resonators are promising candidates for biochemical and gravimetric sensor applications [52, 53, 54, 55] and is currently challenging the mature quartz-based technology in terms of both mass resolution and cost effectiveness. The main advantages of using the thin film technology are (1) the IC-compatible fabrication process, and (2) a much higher operational frequency. By using IC technology to fabricate these sensors, a considerable size reduction of the sensor area by about three orders

of magnitude can be achieved. Since standard planar technology is used, low cost sensor arrays can easily be built which enables a higher throughput for pharmaceutical screening experiments [56]. In addition, the possibility of co-integrating sensors with microelectronic read-out circuitry on the same chip offers oscillator mode operation [57]. The higher operational frequency >1GHz of the thin film sensor technology offers, in theory, a much greater mass sensitivity than that of quartz sensors which operate in the 5-10MHz range. The sensitivity, i.e. the frequency shift per added mass of a single layer resonator is given by [58]:

$$s = \frac{\partial f}{\partial m} = \frac{f_0}{M} \propto -f_0^2, \tag{4.1}$$

where f_0 is the operational frequency and M the mass of the resonator.

Previous work done by our group [55, 59, 6] has studied the use of FBARs gravimetric sensors in liquid environments. The sensing surface typically is the bottom electrode of the FBAR which in turn is fabricated on top of a microfluidic system defined in the Si carrier substrate.

In this thesis, the more robust SMR structure has been studied for biosensor applications. In Paper VII a sensor system based on a thickness shear mode SMR were fabricated. Here, the microfluidic system was defined in a slab of polydimethylsiloxane (PDMS), guiding the liquid over the top electrode of the SMR. PDMS is an elastomeric polymer with the advantage of rapid and less expensive prototyping than micromachining of Si [60]. Furthermore, the surface of the PDMS can be modified to enable bonding with SiO_2.

The fabrication of SMRs for sensors relies on the same principles laid out in Section 2.2. In Paper VII the acoustic mirror was fabricated by three pairs of SiO_2/Mo. In Paper VIII a dielectric SiO_2/AlN mirror was used to prevent further capacitive coupling via the mirror to the ground pads and electrical probes.

Furthermore, in order to operate in liquid, the AlN piezoelectric film was deposited with a mean tilt of the c-axis.

SiO_2-PDMS bonding

The SiO_2 surface is hydrofilic by nature, while the surface of PDMS is hydrophobic. For the PDMS to bond to the SiO_2, its surface must first be modified by oxygen plasma treatment, during which OH-groups are formed on the surface that will bond covalently to the oxide surface when brought into contact. In Paper VIII, the top surface of the resonator is passivated by a thin layer of reactively sputtered SiO_2. When the SiO_2 and the PDMS is put into contact under heat and pressure, the two structures form a irreversible bond. Thus the PDMS slab cannot be removed from the device without breaking.

Q-degrading factors and cross-talk

Q-limiting factors for BAW devices, as discussed in Section 3.2.2, can be divided into electrical and mechanical mechanisms. For BAW sensor applications additional losses associated with the viscous load of the liquid is in-

troduced. Consequently, used as sensor devices have lower Qs than devices operating in air. In this thesis, Q degradation related to the conductivity of the liquid is studied in Paper VIII.

As discussed above, the planar technology enables the formation of sensor arrays for multipurpose detection systems including sensors for in-liquid operation. For such an application it is not unlikely that the substance being analysed is perfectly non-conducting. Within the scope of this thesis, it has been found that the conductivity of the liquid analyte may under certain circumstances greatly affect the performance of the active sensor in a negative manner. In Paper VIII, an analysis of the observed Q-degrading factors [61] and the resonator-resonator crosstalk in such an array of sensors was done. Here the sensing electrodes of two SMRs, in close proximity and operating in the same PDMS microfluidic channel, were exposed to a conductive liquid. It was found that when the signal electrode was in contact with the conductive liquid, additional fringe capacitance and ohmic leakage paths through the liquid to the ground electrode have a negative impact on the resonator performance. For the range of analytes measured, a drop in the Q factor of more than 30% was observed. Furthermore, in the presence of a liquid in the microfluidic channel, the resonator-resonator crosstalk (here represented by the forward voltage gain, S_{21} parameter) increased by 20dB from the level measured in air. The term crosstalk refers to any phenomenon by which a signal transmitted on one circuit of a transmission system creates an undesired effect in another circuit or channel. Crosstalk is usually caused by undesired capacitive, inductive, or conductive coupling from one circuit, part of a circuit to another.

By inverting the resonator topology, i.e. applying the signal to the bottom electrode and grounding the top electrode, the observed energy leakage was limited by a Q factor drop of 9% while no increase in S_{21} could be observed at all. It is noted that in the inverted SMR sensor array, the top electrode was somewhat larger than the bottom electrode,

5. Surface acoustic wave devices

In the same manner as their BAW counterparts, surface acoustic wave (SAW) devices utilise the piezoelectric effect for generation and detection of mechanical waves. The major difference between the two types of waves is that SAWs are guided along the surface of a homogeneous bounded material rather than propagating in the bulk. For a SAW, typically 90% of the wave energy is confined within one wavelength of the surface [62].

A propagating SAW is accompanied by an electric field localised at the surface [63], this enables the wave to effectively be excited using a metal comb-like structure fabricated on top of the piezoelectric material. This common geometry is referred to as an interdigital transducer (IDT) and is shown in Fig. 5.1 (a). The electrode array contains two electrodes per period (wavelength λ), connected to two busbars over which the electrical input signal is applied. The resonance frequency of the SAW is determined by the equation $f = v/\lambda$, where f is the resonance frequency, v is the phase velocity, and λ is the wavelength of the excited wave. Correspondingly, if the frequency of the applied voltage is close to the fundamental wavelength of the SAW, every period in the array will generate a SAW and all these waves sum up in phase.

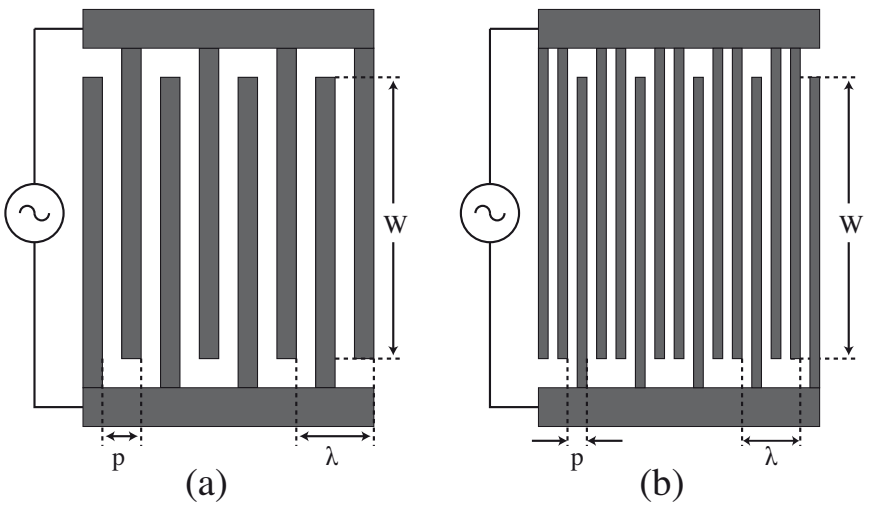

Figure 5.1: (a) Basic geometry of an interdigital transducer (IDT). (b) Multi-electrode design of the IDT for non-reflective devices.

The basic geometry of the IDT is associated with strong internal reflections, which is beneficial if the device is used as a resonator. However, for transducer action, these internal reflections effectively reduce the energy transmitted by the IDT. To remove the internal reflectivity a multi-electrode design, as shown in Fig. 5.1 (b) can be used [64, 65]. The resonance frequency of this geometry is the same as that of the basic geometry, but strong reflections only occur at frequencies far from the centre frequency. The multi-electrode IDT geometry of Fig. 5.1 (b) was used in Paper IX and X. in order to remove reflectivity and maximise the energy transmitted into the micromachined channel. Since half of the energy is transmitted in the opposite direction, a reflector is fabricated on one side of these transducer with a $\lambda/4$ electrode width/spacing in order to reflect that energy in the desired direction. A segment of the actual IDT geometry used is shown in Fig. 5.2.

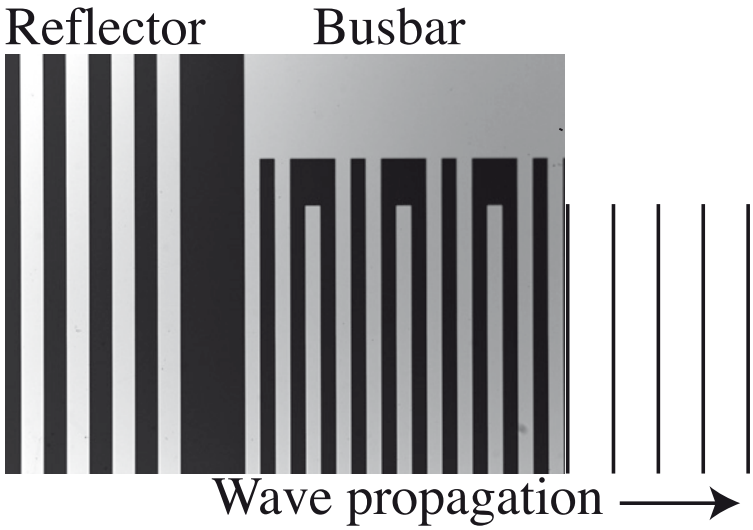

Figure 5.2: Image of Au IDTs fabricated on top of the $LiNbO_3$ substrate in Paper IX. The width of the IDT and electrode-electrode spacing is $16\mu m$ ($\lambda/6$), corresponding to a wavelength of $96\mu m$. The reflector strips is $\lambda/4$, or $24\mu m$ wide. The transducer is 40λ long and 9mm wide. The vertical lines on the right symbolise the wave fronts of the SAW.

SAW devices are fabricated on bulk piezoelectric crystals such as *Quartz*, $LiNbO_3$, and $LiTaO_3$ and typically exhibit phase velocities around 3000m/s. Consequently, most SAW devices fabricated by standard photolithography methods find their use in resonators, oscillators, delay lines and sensors operating in the lower microwave frequency range < 1 Ghz. For the SAW device to operate at higher frequencies, either high resolution lithography is used or the device is fabricated on a high acoustic velocity material. An example of the latter option is realised in Paper II, where a thin piezoelectric AlN film is deposited on a diamond substrate for which the acoustic phase velocity is on the order on 10000m/s.

5.1 Microparticle manipulation

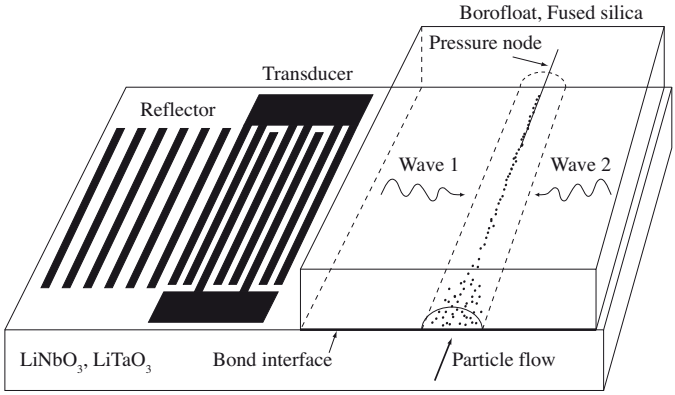

Figure 5.3: Schematic showing the microparticle manipulation device. The second transducer on the right has been left out.

The use of acoustic waves for manipulation of particles with dimension on the order of a few micrometers is of great interest in the biomolecular field where the concept of Lab-on-chip (LOC) and Micro-total analysis systems (μTAS) enable a faster and more cost effective analysis of biological samples [66]

In this thesis, two experimental devices utilising SAWs and interface acoustic waves (IAW) [67], have been developed aiming at extending the use of acoustic waves in sample analysis and microparticle manipulation. The SAW device was based on a Y-cut $LiNbO_3$ substrate bonded together with a piece of Borofloat glass, while the IAW device was fabricated by bonding a X-cut $LiTaO_3$ substrate to a piece of fused silica (SiO_2).

For both devices, schematically shown in Fig. 5.3, two unidirectional interdigital transducers fabricated on the piezoelectric substrate, are used to excite a SAW each propagating in opposite directions toward each other (For the second device, the SAW will subsequently couple to an IAW propagating along the $LiTaO_3/SiO_2$ interface.) Midway between the transducers a microfluidic channel is bonded to the substrate by SU-8 adhesive bonding and in the channel there is a continuous flow of randomly distributed particles. Along the microfluidic channel, the two waves will interfere producing pressure nodes and anti-nodes in the liquid. When the randomly distributed particles enter the force field defined by the aperture of the IDTs, they will be aligned along the pressure node, or anti-node depending on the contrast factor of the particle [68]. The fabricated devices can be used in a wide variety of applications, e.g. increase particle concentration, particle counting, and separation of positive-negative-contrast particles.

The radiative force exerted on the particles, is defined as [69]

$$F_r = -V_p P_0^2 \left(\frac{\pi}{2\rho_0 c_0^3}\right) f\theta(\beta,\rho) \sin\left(2\pi \frac{z}{\lambda/2}\right) \tag{5.1}$$

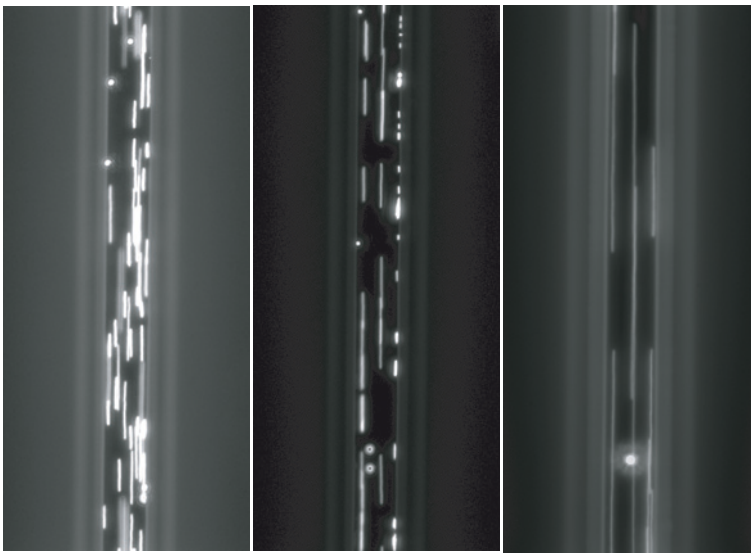

(a) (b) (c)

Figure 5.4: Microparticle flow in the channel over a $LiNbO_3$ substrate. In (a) the IDTs are turned off and the particles (positive-θ) flow at random positions along the channel. In (b) only one IDT is active and (c) both IDTs are turned on with particle alignment along three separate nodes, corresponding to the wavelength in the liquid, can be observed.

$$\theta = \frac{5\rho - 2\rho_0}{2\rho + \rho_0} - \frac{\beta}{\beta_0} \tag{5.2}$$

where V_p is the volume of the particles, P_0 the amplitude of the acoustic pressure oscillations, ρ_0 and c_0 the density and velocity of sound of the medium and ρ the density of the particles. f is the applied frequency. θ is the acoustic contrast factor where β and β_0 is the compressibility of the particle and medium. Depending on the sign of θ, the exerted force may align particles along a pressure node (positive) or an pressure anti-node (negative).

The effect of the acoustic pressure nodes present in the Borofloat glass channel is illustrated in Fig. 5.4. In the image to the left (a), the transducers are turned off to display the random distribution of the 1.9μm particles. When one of the transducers are turned on, as shown in the centre image (b), the particles align along the three pressure nodes present in the channel. With both transducers active (c) the same node pattern can be observed.

The node pattern differs from what has been obtained for other SAW-transducer systems with PDMS channel [70] or without side-walls [71]. The three nodes observed indicate the presence of an acoustic standing wave inside the microfluidic channel, for which the node separation corresponds to the acoustic wavelength in water. As such, the microfluidic channel defines an acoustic resonance cavity. This observation, in addition to the

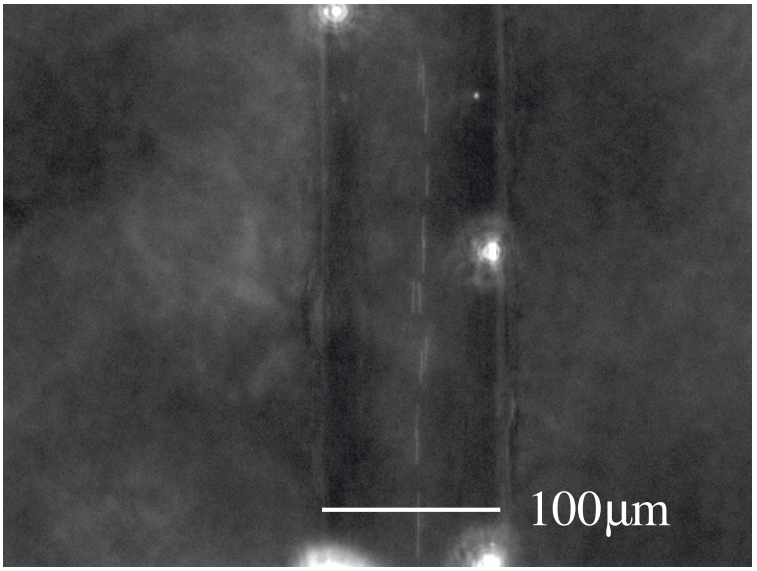

Figure 5.5: Alignment of 0.5 μm particles (positive-θ) using IAW propagating in the $LiTaO_3$/Fused silica interface. Only one pressure node in the 100μm wide channel can be seen. Thus, the spacing of the pressure node is defined by the IAW wavelength in the solid.

possibility of single-IDT operation suggests that the glass structure is the main origin of reflection, rather than counter-propagating waves from the two IDTs. Symmetric node alignment relative to the channel walls supports the glass/fluid interface as a dominating origin of reflection rather than the outer boundaries of the glass structure. The possibility of operation with only one transducer makes the total device smaller.

In the IAW device, a similar geometry and fabrication technique is realised. In this case, the substrate materials is X-cut $LiTaO_3$ and the microfluidic channel is fabricated in fused silica [72, 73]. At the interface formed by the piezoelectric and dielectric substrates, the two counter-propagating SAWs couple to interface acoustic waves (IAW) that propagate without loss along the boundary of the two solid media [74]. It is noted that IAWs only exist under specific conditions which imposes certain restrictions on the choice of materials. Using this device, alignment of sub-μ particles was realised around 35 MHz. An image of the focussed particle beam can be seen Fig. 5.5.

Another feature of the IAW system is its ability to operate by single IDT excitation as well as by excitation with both IDTs connected in series. For the single IDT operation, strong particle alignment is found at 34.2 MHz, while for the case when both IDTs are operated strong particle manipulation is observed at 34.6 MHz. It is noted that most generally the alignment frequencies for both excitation geometries (i.e single IDT and both IDTs in series) do not coincide. The latter is thought to originate from the different phase conditions

determined by the non-symmetrical alignment of the channel with respect to the transducers.

It is further noted here, that the single node of operation observed in Fig. 5.5 indicates that the acoustic wavelength in the microfluidic channel is in excess of 100 μm. This yields an acoustic wave velocity in the channel slightly higher than 3400 m/s. Note that the interface wave at the SiO_2/X-cut $LiTaO_3$ boundary has an acoustic wave velocity of 3500 m/s. Thus, the presence of the fluid into the channel has just a perturbing effect on the IAW. Most generally, when the wave is de-coupled at the surface, the nodes separation is determined by the speed of sound in the fluid yielding λ=44μm in this case, which is not experimentally observed.

5.1.1 Device fabrication

The transducers

One of the advantages of SAW device fabrication is the relatively simple electrode definition, requiring only one mask step. In this work, the Au electrodes were patterned, using a lift-off process since it does not require the explicit use of a Au-etchant. Since Au does not adhere well to oxides, a thin Ti layer was first deposited to enhance metal/substrate adhesion. The metals were deposited by resistive evaporation with a base pressure in the range of 10^{-5} to 10^{-6} mBar. Immediately after metal deposition, the wafers were immersed in acetone with applied ultrasound to remove the excess metal and photoresist

The microfluidic channel

Fabrication of the microfluidic channels in the Borofloat glass and fused silica substrates were not as straightforward. It is a well known fact that hydrofluoric acid (HF 50 %) is a suitable wet etchant for SiO_2, Pyrex, fused silica, etc. since it provides room-temperature etching at relatively high rates [75]. For etching of glasses with a lot of metal impurities, metal-oxides insoluble in HF will cause significant micromasking. This phenomenon can be circumvented by applying a ultrasonic treatment at regular intervals. However, this treatment put a lot of strain on the masking material. Instead, hydrochloric acid can be added to the etch with a ratio (10:1) to render some of the metal oxides soluble [76]. However, given the relatively deep channel structures (20 - 60 μm), the range of masking materials is quite short. Among the hard mask materials suggested in the literature (and available in our lab) poly-Si and Au have provided the best results [76, 77].

For the Borofloat substrate, a 500 nm Au mask with a Ti adhesion layer was chosen since we did not have access to a non-CMOS LPCVD to fabricate a poly-Si mask. The Au mask was deposited by e-beam evaporation in intervals of 100 nm at a time with a 20 minute waiting time in between depositions. This prevents pinholes in the Au mask to appear as the mask cools down [75]. In addition, the temperature of the poly-Si deposition process is 650°C which is above the anneal/re-flow temperature of the glass substrate. Thus, at this temperature, the risk of substrate bending is high. After mask deposition

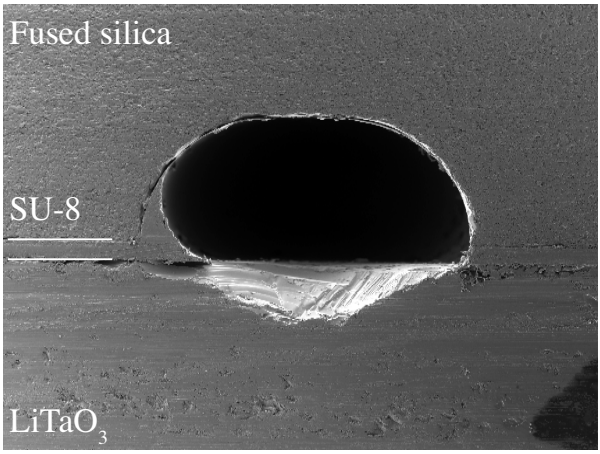

Figure 5.6: SEM micrograph of the adhesively bonded $LiTaO_3$/fused silica interface. The thickness of the SU-8 is about 5μm. The width and height of the channel is 100μm by 40μm. The wave shape on the left side of the channel is due to sliding of the silica piece during the manual bond process.

and patterning, the glass substrate must be protected from the backside during etching. Here, this was done by applying a sufficiently wide and thick tape. The etch rate of Borofloat silicate glass in HF(50%)/HCl(37%) was about 8.5 μm/min which means an etching time of three minutes for a 20 μm deep channel free from pinholes. It is noted here that the 10 μm thick photoresist used to pattern the Au mask was not removed from the substrate prior to the etch and a proper evaluation of the Au mask can therefore not be done.

For the fused silica substrate, on the other hand, deposition of a 900 nm thick poly-Si mask was straightforward. Using this mask simplifies the process since no HCl additive is required for the etch and since the mask covers the whole substrate, no tape is needed. The poly-Si mask was patterned using a standard Si DRIE-etching with a photoresist mask. The fused silica was etched in a HF 50% solution at room temperature with an approximate etch rate of 1.6 μm/min. 25 minutes etching with an occasional stir, resulted in a 40 μm deep and 100 μm wide channel. The p-Si hard mask was then removed in a Tetramethylammonium hydroxide (TMAH) 25%*wt* etch bath heated to 50°C.

To fabricate the through-wafer vias for the fluid inlet and outlet, a 1 mm diamond-tipped drill was used for both types of substrates. At this point, both the piezoelectric substrates and the glasses were diced with a wafer saw to simplify the bonding sequence.

SU-8 Bonding

Prior to SU-8 deposition, the $LiTaO_3$ and silica pieces were heated to 200°C for at least 5 minutes to dehydrate the surface and promote resist adhesion. The SU-8 5 was spun on to the $LiTaO_3$ and $LiNbO_3$ at 4000 rpm for 30 seconds

resulting in a 4 μm thick layer. To reduce the height of the edge bead around the chip, they were left to rest for 30 minutes on a flat surface [78]. During this wait time, the surface of the SU-8 is dries up, which allows for a more accurate placement of the silica chip between the transducers. The glass piece was fitted onto the piezoelectric substrate and pressed together lightly with tweezers, forming an initial bond. This was done before any high temperature treatment was performed on the SU-8 layer. In order to soften the SU-8 5 and thus promote a void free bond, the chip was placed on a hot plate heated to 65°C. During this treatment, the silica/piezo bond was sealed across the entire surface by further pressing the pieces together with tweezers. After forming the bond, the SU-8 5 was exposed through a hard mask to further cross-link the adhesive. After this exposure, the SU8-5 that was covering the IDT's was removed using developer and isopropanol. Last, a five minute post exposure bake at 65°C was done to further strengthen the adhesive bond. To properly determine the strength of the bond requires rather extensive and complicated testing. Here, the absolute strength of the bond is of secondary importance with the only requirement to provide a bond strong enough for the application. It is, however, pointed out that after the above described process, the bond could not be broken without breaking either of the substrates, thus destroying the device.

A SEM micrograph of the bonded $LiTaO_3$ and fused silica interface can be seen in Fig. 5.6.

6. Summary of Appended Papers

Paper I

"Solidly mounted thin film electroacoustic resonator utilizing a conductive Bragg reflector"

In Paper I, a new configuration of the solidly mounted resonator is proposed. The bottom electrode, which usually constitutes a portion of the acoustic resonance volume, is embedded into the conducting Bragg reflector by using low impedance aluminium instead of SiO_2. The advantages of the proposed design include reduced series resistance, utilization of the full piezoelectric coupling at higher frequencies, higher power handling capabilities, and improved heat conductivity. A device based on the proposed design is fabricated and the performance compared with a resonator fabricated according to the standard model. The improvement in Q value due to a reduction in series resistance is experimentally verified. Furthermore, a linear model for extracting the electrical components of the BVD model in resonators with strongly dispersive lateral modes is introduced. My contribution to this work was the idea, the fabrication, and the measurements of the devices.

Paper II

Design of high frequency piezoelectric resonators utilizing laterally propagating fast modes in thin aluminum nitride (AlN) films."

This paper explores the potential of FPAR, using Lamb waves in AlN based electroacoustic applications. In order to demonstrate the advantage of using Lamb wave devices over SAW devices, a comparative study between the two technologies is done. The SAW device is fabricated on a Diamond /Si substrate with a top layer of AlN whereas the Lamb device is fabricated on plain Si wafer. Both devices have a resonance frequency around 1Ghz but the Q·f product of the Lamb device is about three times higher than that of the SAW device which clearly demonstrates the big potential of the proposed technology. I contributed with the fabrication of the FPAR devices in this paper.

Paper III

"Electric Field Sensitivity of Thin Film Resonators Based on Piezoelectric AlN Thin Films"

The purpose of Paper III is to examine the DC electric field sensitivity of the AlN based FBAR, SMR, and FPAR. When a DC bias voltage is applied to the signal electrode of the resonator, a frequency shift can be observed. The three contributors to the frequency shift are changes in density, film thickness, and the elastic constants. In this study it is found that the stress-strain induced elastic constant shift of the piezoelectric film has a predominant role over the device sensitivity and that the longitudinal and shear moduli exhibit opposite pressure coefficients. The FBAR has a higher sensitivity for both longitudinal and shear waves compared to the SMR. The sensitivity of the FPAR can be increased by applying the same bias voltage to the distributed reflectors. In this work, I fabricated the SMRs, the FPAR with biased reflectors, and did all the measurements.

Paper IV

"Thick silicides synthesised with smooth surface for integrated TFBAR applications"

In Paper IV, the fabrication process and potential applications of thick NiSi is described. To show the potential of using NiSi electrodes in electroacoustic devices, a comparative study is done between FBARs having Mo electrodes and NiSi top electrodes. To form the thick NiSi layer, a sequence of Ni and Si thin films are de-posited to form a multilayered stack which then is annealed at 500°C. Using this method, it was found that arbitrarily thick NiSi films can be fabricated by conventional DC sputtering. Fabricated FBARs show comparable performance in coupling coefficient around 3.6% and a parallel Q of 600. Due to the larger series resistance of NiSi, the series Q factor is lower than that of Mo-electrode FBAR. The study shows that using as electrode material is a viable technology if the series resistance can be reduced further. For high power applications, a theoretical study of using NiSi and Ir in a conductive Bragg reflector is performed. In this work, I contributed with a preliminary study of Ni silicidation and AlN growth on NiSi. I was also involved in the technical discussions of the project.

Paper V

"A 2Ghz oscillator based on a solidly mounted thin film bulk acoustic wave resonator."

Paper V describes our first attempt of integrating a solidly mounted resonator with the passive and active IC-components of an oscillator. Since a monolithic integration of all components is very difficult, this attempt used a patterned dielectric substrated on which the discreet components were mounted. The SMR used for the oscillator had a SiO2/Mo Bragg reflector

and aluminum electrodes. The SMR chip was "diced" using DRIE of the Si substrate. The output frequency of the oscillator was 2 GHz and output power of 0 dBm. My contribution to this work was the design of the process flow and the fabrication of the SMR used in the oscillator.

Paper VI

Oscillators based on monolithically integrated AlN TFBARs"

Paper VI describes our second attempt to integrate a solidly mounted resonator in an oscillator. The idea of this paper is to fabricate the oscillator as a multi-chip module where the passive elements of the device are fabricated on a low-loss substrate and the active element is mounted by flip-chip technology to make the final device. In this work, the substrate is a high resistivity Si-wafer with a dielectric AlN/SiO2 Bragg reflector deposited on one side. A separate study was made in advance to determine the specific impedance of coplanar transmission lines. On top of this susbstrate the resonator was fabricated. The top metal layer of the device contained the distributed components and the impedance matched transmission lines of the oscillator. My contribution to this work was the idea and to fabricate the oscillator.

Paper VII

Fabrication and characterization of a shear mode AlN solidly mounted resonator-silicone microfluidic system for in-liquid sensor applications

In this paper, a process for the fabrication of an in-liquid sensor system based on the solidly mounted resonator is presented. A SMR operating in the shear mode, with a tilted AlN film and a SiO_2/Mo Bragg reflector is fabricated. On top of the SMR structure a thin layer of SiO_2 is deposited which enables a microfluidic system defined in a slab of PDMS to be bonded to the SMR device. Shear mode excitation enables the SMR to operate in liquid environments with minimal acoustic loss. The sensor was operated and characterised in air, de-ionised water, glycerol, and acetone. The resonance frequency was around 1.2 GHz with a Q factor of 100 in water. In this work I contributed in the technical discussions and the fabrication of the SMR-sensors.

Paper VIII

"Analysis of Q-degradation and cross-talk in BAW sensor arrays operating in conductive liquid media"

In this paper, two sensor arrays based on shear mode thin film bulk acoustic resonators fabricated in the SMR configuration on a dielectric Bragg reflector, together with a PDMS microfluidic transport system is presented. The resonators have operating frequencies of 1.3Ghz with a Q value of 180 in deionized water. As the conductivity of the liquid over the resonators increases, a significant decrease in the Q factor for the first type of sensor array can be observed while the second type only shows little Q reduction. This is explained

by the additional fringe capacitance and ohmic leakage paths through the liquid present in the first array, when the signal electrode is in contact with the latter. By applying the signal to the bottom electrode and grounding the top (sensing) electrode, the reduction in Q is minimised and no cross-talk can be observed. In this work I contributed with the fabrication, measurements, and data analysis.

Paper IX

"Surface acoustic wave-excited particle manipulation in a glass microfluidic channel"

In Paper IX, the fabrication and characterisation of a micro-particle manipulation device is presented. The device consist of a bulk piezoelectric $LiNbO_3$ substrate and a microfluidic system fabricated in a piece of Borofloat glass. The two different substrates are bonded together using SU-8 adhesive bonding.

Surface acoustic waves are excited on the $LiNbO_3$ by two unidirectional IDTs operating at 35.6 MHz. These waves propagate in opposite directions and interfere in the center to create a standing pressure gradient along the microfluidic channel. The pressure gradient force positive-θ particles (1.9 μm diameter) transported in the channel to align along three pressure nodes indicating a de-coupling of the acoustic wave into the water. The separation of the nodes in the direction of propagation, thus correspond to $\lambda/2$ of the applied frequency in water. As a consequence, particle manipulation could be realised using only one of the IDTs. My contribution was to design the process flow and to fabricate the devices.

Paper X

Interface acoustic wave based particle manipulation in microfluidics channels.

In this paper, a microfluidic device similar to that of Paper IX is fabricated. The major difference is that another type of wave is excited. Although the transducers are the same, as the SAW propagates into the bonded microfluidic chip, it will couple to an interface acoustic wave propagating along the piezoelectric/glass interface. IAW only exist for certain combinations of materials. In this case a X-cut $LiTaO_3$ and a fused silica substrate was chosen. The IAW propagates in the pure Z-direction. Microparticle manipulation of polystyrene beads with a diameter of 0.5μm was realised. The operation frequency of the transducers was about 35MHz, but only one pressure node could be observed in the channel. This suggests that the position of the nodes are not determined by the acoustic wavelength in water but rather that of the bulk $LiTaO_3$. My contribution was to design the process flow and to fabricate the devices.

7. Sammanfattning på svenska

Denna avhandling behandlar design, tillverkning och karakterisering av elektroakustiska komponenter som kan integreras med annan elektronik. Under de senaste trettio åren har forskningen inom detta område varit en kraftigt bidragande faktor till dagens multifunktionella mobiltelefoner och att många andra enheter för trådlös kommunikation har letat sig in i folkhemmet. Idag läggs även stora resurser på att identifiera andra områden där elektroakustiken kan utnyttjas. Ett sådant område är sensorer för biologiska mätningar.

En elektroakustisk komponent konverterar en elektrisk signal till en mekanisk (akustisk) våg och vice versa. Detta kan den göra eftersom komponenten delvis består av ett piezoelektriskt material som blir elektriskt polariserat vid yttre kraftpåverkan. På motsvarande sätt kan materialet utvidgas/komprimeras av ett elektriskt fält.

En elektroakustisk komponent består av en resonanskavitet, en s.k. *resonator* som i dess enklaste form består av en tunn piezoelektrisk film med en tunn elektrod på vardera sida. Om en lågfrekvent signal läggs mellan elektroderna, uppför sig resonatorn som en kondensator. Om frekvensen på signalen ökar så att våglängden på de mekaniska vågor som signalen exiterar mellan elektroderna, är dubbelt så lång som tjockleken på den piezoelektriska filmen, kommer resonatorn i "resonans" och den kortsluts. Som sådan kan resonatorn användas för att bygga mycket små signalfilter radio- och mikrovågstillämpningar.

I avhandlingen behandlas tre typer av resonatorer som alla tillverkats i renrummet på Ångströmlaboratoriet i Uppsala. Den första typen av resonator är den s.k. membranresonatorn (FBAR) där resonanskaviteten tillverkats på ett kiselsubstrat. Substratet under kaviteten etsas sedan bort vilket frilägger membranet. Den andra typen är den s.k. ytmonterade resonatorn (SMR) där resonatorn isoleras från substratet med hjälp av en akustisk spegel (reflektor.) Den tredje typen kallas FPAR och består likt FBAR av ett tunt membran. I denna typ av resonatorn fortplantar sig den akustiska vågen vinkelrätt mot det elektriska fältet. En schematiska skiss av dessa resonatorer kan ses i figur 2.1.

Avhandlingen består av åtta vetenskapliga rapporter som behandlar olika aspekter av design, tillverkning, karakterisering och integrering av elektroakustiska komponenter tillverkade med tunnfilmsteknik. I dessa rapporter behandlas bulk-akustiska vågor. Ytterligare två rapporter behandlar komponenter tillverkade på piezoelektriska substrat. Dessa rapporter behandlar yt-akustiska vågor.

I den första rapporten presenteras en konceptuellt ny design av den s.k. ytmonterade resonatorn. Där elektroderna har integrerats i den akustiska spegel

som reflekterar energi tillbaka till resonatorn. En jämförande studie visade att Q-värdet i denna typ av resonatorer är högre än in motsvarande resonator med tunna elektroder. Denna design kan även visa sig lämplig för resonatorer för högre frekvenser (> 10 GHz) eftersom serieresistansen i elektroderna inte längre begränsar Q värdet.

Den andra rapporten är en jämförande studie av en resonator (FPAR) där en akustiska vågen fortplantar sig i ett membran vinkelrätt mot det elektriska fältet (en s.k. Lamb-våg) och en yt-akustisk resonator (SAW). Båda resonatornerna har i studien en resonansfrekvens nära 1 GHz. FPAR består av ett tunt membran av aluminiumnitrid som frilagts på ett kiselsubstrat. SAW-resonatorn tillverkades på ett specialsubstrat bestående av aluminiumnitrid/diamant/kisel. våghastigheten i de båda resonatorerna ligger runt 10000m/s. Studien visar på några av de fördelar som Lamb-vågor bidrar med jämfört med ytvågor. Bl.a. erhölls ett högre Q värde på 2000 för FPAR jämfört med 600 för SAW. En FPAR kan dessutom tillverkas på billiga kiselsubstrat istället för specialsubstrat som i fallet med SAW. Dessutom innebär den höga våghastigheten att resonatorer upp till 5GHz kan tillverkas med konventionell fotolitografi.

I den tredje rapporten undersöks vad som händer med resonansfrekvensen när ett statiskt elektriskt fält (bias) läggs mellan elektroderna. Tre typer av resonatorer undersöks (FBAR, SMR och FPAR.) När en bias läggs mellan elektroderna flyttas resonansfrekvensen så pass mycket att det inte enbart kan förklaras av volymförändringar i materialet. Studien identifierar den störst bidragande faktorn till frekvensskiftet som icke-linjära förändringar i materialets styvhetstensor. För den longitudinella moden blir materialet styvare vilket resulterar i ett positivt frekvenskift. För den transversella moden är skiftet negativt.

Den fjärde rapporten beskriver en tillverkningsprocess för godtyckligt tjocka nickelsilicider (NiSi). NiSi är en lågresistiv silicid som skulle kunna ersätta Al som elektrod i resonatorn. Som sådan skulle effekt- och temperaturtåligheten i resonatorn öka. I studien jämförs FBAR med NiSi elektroder och Mo elektroder.

Den femte och sjätte rapporten behandlar ytmonterade resonatorer integrerade i mikrovågsoscillatorer med en utfrekvens runt 2 GHz. Två olika integreringskoncept behandlas. Den första oscillatorn är monterad på ett mikrovågssubstrat medan den andra är monolitiskt integrerad i ett specialtillverkat substrat. Den aktiva komponenten i oscillatorerna är ytmonterade bipolära transistorer.

I den sjunde och åttonde rapporten utvecklas ytmonterade resonatorer för sensorapplikationer. I dessa resonatorer är kristallstrukturen i den piezoelektriska aluminiumnitriden roterad så att den transversella moden kan exiteras. Detta gör att resonatorn kan fungera även nedsänkt i en vätska. I rapporterna har ett mikrofluidisk kanal monterats ovanpå resonatorn och den ena elektroden. Vätskor med olika viskositeter flödas över elektroden vilket gör att resonansfrekvensen sjunker. Om vätskan innehåller joner kan den även orsaka

parasitiska kopplingar mellan signal och jord. I åttonde rapporten presenteras hur detta skall undvikas.

Avhandlingens två sista rapporter studerar hur akustiska vågor skall kunna utnyttjas för att manipulera mikropartiklar som transporteras i ett kanalsystem. En mikrofluidisk kanal i glass och en i kvarts tillverkades och monterades sedan på ett var sitt piezoelektriskt substrat genom klisterbondning. Glaskomponenten utnyttjar två yt-akustiska vågor som sammanfaller konstruktivt i kanalen. Detta resulterar i att en stående våg etableras i kanalen som bidrar med kraftverkan på partiklarna i kanalen. Partiklarna med en diameter på 1.9 mikrometer samlas därför längs en av dessa noder till en samlad partikelstråle.

Samma koncept utnyttjas även i den tionde rapporten fast där med en annan typ av våg: en gränssnittsvåg. Denna våg är något mer effektiv då energiförlusterna hos vågen är små. Samma kraftverkan på partiklarna kunde påvisas även här, fast för mycket mindre partiklar med en diameter på 0.5 mikrometer.

Acknowledgements

Nanos gigantum humeris insidentes

A doctoral thesis is seldom a product of the work put down by one person. This thesis is no exception. Many people have contributed to this work and for this they are gratefully acknowledged. I want to thank...

...my supervisor *Ilia Katardjiev* for granting me the challenge of putting together a Ph.D.

...*Ventsislav Yantchev* for knowing everything about electroacoustics.

...*David Martin* for being a good travel companion.

...*Johan Bjurström* for being another good travel companion.

...the indispensable *Marianne Asplund* for being the spider in the web.

...*Olof Bengtsson* for helping out with the power measurements.

...*Jörgen Olsson* for taking me in as an "exjobbare."

...*Lars Vestling* for talking UNIX with me.

...*Linda Johansson* for an interesting yet tough collaboration towards the end.

...all the other colleagues at SSE for all the lovely luncheons.

...the MSL staff for being on the alert whenever I needed you and for fixing all the machines I broke. Your work will ease up now that I'm gone.

...*Martin Norling* and *Spartak Gevorgian* for a successful collaboration in the ICTEA-project.

...my gorgeous family *Erika*, *Elsa*, and *Albin*.

Johannes Enlund
Mars 2009

Bibliography

[1] http://www.eetimes.com/showarticle.jhtml?articleid=188500206&pgno=2.

[2] B.A. Auld. *Acoustic Fields and Waves in Solids*. Robert E. Krieger Publishing Company Inc., 2nd edition, 1990.

[3] Joel F. Rosenbaum. *Bulk Acoustic Wave Theory and Devices*. Artech House, 1988.

[4] K. Tsubouchi, K. Sugai, and N. Mikoshiba. Aln material constants evaluation and saw properties on aln/al2o3and aln/si. *Ultrasonics Symposium*, pages 375–380, 1981.

[5] K. Tsubouchi, K. Sugai, and N. Mikoshiba. Zero temperature coefficient surface-acoustic-wave devices using epitaxial aln films. *Ultrasonics Symposium*, pages 340–345, 1982.

[6] J. Bjurstrom, G. Wingqvist, V. Yantchev, and I. Katardjiev. Temperature compensation of liquid fbar sensors. *Journal of Micromechanics and Microengineering*, 17(3):651 – 658, 2007.

[7] R.C. Ruby, P. Bradley, Y. Oshmyansky, A. Chien, and III Larson, J.D. Thin film bulk wave acoustic resonators (fbar) for wireless applications. *Ultrasonics Symposium, 2001 IEEE*, 1:813–821, 2001.

[8] J.S. Wang and K.M. Lakin. Sputtered aln films for bulk-acoustic-wave devices. *1981 Ultrasonics Symposium*, pages 502–505, 1981.

[9] K.M. Lakin, J.S. Wang, G.R. Kline, A.R. Landin, Y.Y. Chen, and J.D. Hunt. Thin film resonators and filters. *1982 Ultrasonics Symposium*, pages 466–475, 1982.

[10] W.E. Newell. Face-mounted piezoelectric resonators. *Proceedings of the IEEE*, 53(6):575 – 581, 1965.

[11] K.M. Lakin, K.T. McCarron, and R.E. Rose. Solidly mounted resonators and filters. *Proceedings of the IEEE Ultrasonics Symposium*, 2:905 – 908, 1995.

[12] M.-A. Dubois, P. Muralt, H. Matsumoto, and V. Plessky. Solidly mounted resonator based on aluminum nitride thin film. *Ultrasonics Symposium, 1998. Proceedings., 1998 IEEE*, 1:909–912, 1998.

[13] S. Marksteiner, J. Kaitila, G.G. Fattinger, and R. Aigner. Optimization of acoustic mirrors for solidly mounted baw resonators. *Ultrasonics Symposium, 2005 IEEE*, 1:329–332, Sept. 2005.

[14] G.G. Fattinger, S. Marksteiner, J. Kaitila, and R. Aigner. Optimization of acoustic dispersion for high performance thin film baw resonators. *Ultrasonics Symposium, 2005 IEEE*, 2:1175–1178, Sept. 2005.

[15] R. Thalhammer, J. Kaitila, S. Zieglmeier, and L. Elbrecht. Spurious mode suppression in baw resonators. *Ultrasonics Symposium, 2006. IEEE*, pages 456–459, 2006.

[16] R. Lanz, M.-A. Dubois, and P. Muralt. Solidly mounted baw filters for the 6 to 8 ghz range based on aln thin films. *Ultrasonics Symposium, 2001 IEEE*, 1:843–846, 2001.

[17] K.M. Lakin, J. Belsick, J.F. McDonald, and K.T. McCarron. Improved bulk wave resonator coupling coefficient for wide bandwidth filters. *Ultrasonics Symposium, 2001 IEEE*, pages 827–831 vol.1, 2001.

[18] J. Bjurstrom, V. Yantchev, and I. Katardjiev. Thin film lamb wave resonant structures - the first approach. *Solid-State Electronics*, 50(3):322 – 6, 2006.

[19] V. Yantchev and I. Katardjiev. Thin aln film resonators utilizing the lowest order symmetric lamb mode: Further developments. *Frequency Control Symposium, 2007 Joint with the 21st European Frequency and Time Forum. IEEE International*, pages 1067–1072, 2007.

[20] W.P.; Mason, editor. *Electromechanical transducers and wave filters*. New York, D. Van Nostrand Co., Toronto, Canada, 1948.

[21] W.P. Mason. Physical acoustics and the properties of solids. *Journal of the Acoustical Society of America*, 28(6):1197 – 1206, 1956.

[22] H. Nowotny and E. Benes. General one-dimensional treatment of the layered piezoelectric resonator with two electrodes. *Journal of the Acoustical Society of America*, 82(2):513 – 21, 1987.

[23] H. Nowotny, E. Benes, and M. Schmid. Layered piezoelectric resonators with an arbitrary number of electrodes (general one-dimensional treatment). *Journal of the Acoustical Society of America*, 90(3):1238 – 45, 1991.

[24] III. Larson, J.D., P.D. Bradley, S. Wartenberg, and R.C. Ruby. Modified butterworth-van dyke circuit for fbar resonators and automated measurement system. *Ultrasonics Symposium, 2000 IEEE*, 1:863–868 vol.1, Oct 2000.

[25] P. Martin, P. Muralt, M. Cantoni, and M.-A. Dubois. Re-growth of c-axis oriented aln thin films. *2004 IEEE Ultrasonics Symposium (IEEE Cat. No.04CH37553)*, Vol.1:169 – 72, 2004.

[26] F. Engelmark, G.F. Iriarte, I.V. Katardjiev, M. Ottosson, P. Muralt, and S. Berg. Structural and electroacoustic studies of aln thin films during low temperature radio frequency sputter deposition. *Journal of Vacuum Science and Technology, Part A: Vacuum, Surfaces and Films*, 19(5):2664 – 2669, 2001.

[27] F. Martin, P. Muralt, M.-A. Dubois, and A. Pezous. Thickness dependence of the properties of highly c-axis textured aln thin films. *Journal of Vacuum Science and Technology A (Vacuum, Surfaces, and Films)*, 22(2):361 – 5, 2004.

[28] Gonzalo Fuentes Iriarte. *AlN Thin Film Electroacoustic Devices*. PhD thesis, Uppsala University, Solid State Electronics, 2003.

[29] Fredrik Engelmark. *AlN and High-k Thin Films for IC and Electroacoustic Applications*. PhD thesis, Uppsala University, Materials Science, 2002.

[30] Johan Bjurstrom. *Advanced Thin Film Electroacoustic Devices*. PhD thesis, Uppsala University, Department of Engineering Sciences, 2007.

[31] J. Bjurstrom, G. Wingqvist, and I. Katardjiev. Synthesis of textured thin piezoelectric aln films with a nonzero c-axis mean tilt for the fabrication of shear mode resonators. *Ultrasonics, Ferroelectrics and Frequency Control, IEEE Transactions on*, 53(11):2095–2100, November 2006.

[32] M.-A. Dubois, J.-F. Carpentier, P. Vincent, C. Billard, G. Parat, C. Muller, P. Ancey, and P. Conti. Monolithic above-ic resonator technology for integrated architectures in mobile and wireless communication. *IEEE Journal of Solid-State Circuits*, 41(1):7 – 16, 2006.

[33] R. J. Shul, C. G. Willison, M. M. Bridges, J. Han, J. W. Lee, S. J. Pearton, C. R. Abernathy, J. D. MacKenzie, S. M. Donovan, L. Zhang, and L. F. Lester. Selective inductively coupled plasma etching of group-iii nitrides in cl_2- and bcl_3-based plasmas. *Papers from the 44th national symposium of the AVS*, 16(3):1621–1626, 1998.

[34] F. Engelmark, G. F. Iriarte, and I. V. Katardjiev. Selective etching of al/aln structures for metallization of surface acoustic wave devices. *Journal of Vacuum Science & Technology B: Microelectronics and Nanometer Structures*, 20(3):843–848, 2002.

[35] J. R. Mileham, S. J. Pearton, C. R. Abernathy, J. D. MacKenzie, R. J. Shul, and S. P. Kilcoyne. Wet chemical etching of aln. *Applied Physics Letters*, 67(8):1119–1121, 1995.

[36] J.H. Edgar D. Zhuang. Wet etching of gan, aln, and sic: a review. *Materials Science and Engineering: R: Reports*, 48(1):1 – 46, 2005.

[37] Application note. Agilent an 154s-parameter design. *http://cp.literature.agilent.com/litweb/pdf/5952-1087.pdf*, 2006.

[38] J. Kaitila. Review of wave propagation in baw thin film devices - progress and prospects. *Ultrasonics Symposium, 2007. IEEE*, pages 120–129, 2007.

[39] R. Ruby. Review and comparison of bulk acoustic wave fbar, smr technology. *Ultrasonics Symposium, 2007. IEEE*, pages 1029–1040, Oct. 2007.

[40] J. A. Ruffner, P. G. Clem, B. A. Tuttle, D. Dimos, and D. M. Gonzales. Effect of substrate composition on the piezoelectric response of reactively sputtered aln thin films. *Thin Solid Films*, 354(1-2):256 – 261, 1999.

[41] G.F. Iriarte, J. Bjurstrom, J. Westlinder, F. Engelmark, and I.V. Katardjiev. Synthesis of c-axis-oriented aln thin films on high-conducting layers: Al, mo, ti, tin, and ni. *IEEE Transactions on Ultrasonics, Ferroelectrics and Frequency Control*, 52(7):1170 – 4, 2005.

[42] III. Larson, J.D., III Ruby, J.D., R.C. Bradley, J. Wen, Shong-Lam Kok, and A. Chien. Power handling and temperature coefficient studies in fbar duplexers for the 1900 mhz pcs band. *Ultrasonics Symposium, 2000 IEEE*, 1:869–874 vol.1, Oct 2000.

[43] Robert Aigner, Ngoc-Hoa Huynh, Martin Handtmann, and Stephan Marksteiner. Behavior of baw devices at high power levels. *IEEE MTT-S International Microwave Symposium Digest*, pages 429 – 432, 2005.

[44] K.B. Ostman, S.T. Sipila, I.S. Uzunov, and N.T. Tchamov. Novel vco architecture using series above-ic fbar and parallel lc resonance. *Solid-State Circuits, IEEE Journal of*, 41(10):2248–2256, 2006.

[45] M. Norling, D. Kuylenstierna, A. Vorobiev, K. Reimann, D. Lederer, J.-P. Raskin, and S. Gevorgian. Comparison of high-resistivity silicon surface passivation methods. *2007 European Microwave Integrated Circuits Conference*, pages 215 – 18, 2007.

[46] Wei Pang, R.C. Ruby, R. Parker, P.W. Fisher, M.A. Unkrich, and J.D. Larson. A temperature-stable film bulk acoustic wave oscillator. *Electron Device Letters, IEEE*, 29(4):315–318, 2008.

[47] B.P. Otis and J.M. Rabaey. A 300-μw 1.9-ghz cmos oscillator utilizing micromachined resonators. *Solid-State Circuits, IEEE Journal of*, 38(7):1271–1274, 2003.

[48] S.G. Burns, R.J. Weber, and S.D. Braymen. High frequency oscillators using cointegrated baw thin-film piezoelectrics with microwave bjts. *Frequency Control, 1991., Proceedings of the 45th Annual Symposium on*, pages 207–211, 1991.

[49] David M. Pozar. *Microwave Engineering*. Wiley, 3rd edition, 2004.

[50] S.D. MacPherson. High frequency oscillator design using the technique of negative resistance. *AFRICON, 1999 IEEE*, 2:1111–1114, 1999.

[51] D.B. Leeson. A simple model of feedback oscillator noise spectrum. *Proceedings of the IEEE*, 54(2):329–330, 1966.

[52] R. Gabl, E. Green, M. Schreiter, H.D. Feucht, H. Zeininger, R. Primig, D. Pitzer, G. Eckstein, and W. Wersing. Novel integrated fbar sensors: a universal technology platform for bio- and gas-detection. *Sensors, 2003. Proceedings of IEEE*, 2:1184–1188, 2003.

[53] R. Gabl, H.-D. Feucht, H. Zeininger, G. Eckstein, M. Schreiter, R. Primig, D. Pitzer, and W. Wersing. First results on label-free detection of dna and protein molecules using a novel integrated sensor technology based on gravimetric detection principles. *Biosensors and Bioelectronics*, 19(6):615 – 20, 2004.

[54] M. Link, M. Schreiter, J. Weber, R. Primig, D. Pitzer, and R. Gabl. Solidly mounted zno shear mode film bulk acoustic resonators for sensing applications in liquids. *Ultrasonics, Ferroelectrics and Frequency Control, IEEE Transactions on*, 53(2):492–496, 2006.

[55] G. Wingqvist, J. Bjurstom, A.-C. Hellgren, and I. Katardjiev. Immunosensor utilizing a shear mode thin film bulk acoustic sensor. *Sensors and Actuators: B. Chemical*, 127(1):248 – 52, 2007.

[56] R. Brederlow, S. Zauner, A.L. Scholtz, K. Aufinger, W. Simburger, C. Paulus, A. Martin, M. Fritz, H.-J. Timme, H. Heiss, S. Marksteiner, L. Elbrecht, R. Aigner, and R. Thewes. Biochemical sensors based on bulk acoustic wave resonators. *IEEE International Electron Devices Meeting 2003*, pages 32 – 7, 2003.

[57] E. Benes, M. Groschl, W. Burger, and M. Schmid. Sensors based on piezoelectric resonators. *Sensors and Actuators A (Physical)*, A48(1):1 – 21, 1995.

[58] G. Sauerbrey. Use of crystal oscillators for weighing thin films and for microweighing. *Zeitschrift fuer Physik*, 155(2):206 – 222, 1959.

[59] G. Wingqvist, J. Bjurstrom, L. Liljeholm, V. Yantchev, and I. Katardjiev. Shear mode aln thin film electro-acoustic resonant sensor operation in viscous media. *Sensors and Actuators B (Chemical)*, 123(1):466 – 73, 2007/04/10.

[60] Sara Thorslund. *Microfluidics in Surface Modified PDMS : Towards Miniaturized Diagnostic Tools*. PhD thesis, Uppsala University, Department of Engineering Sciences, 2006.

[61] Michael Rodahl, Fredrik Hook, and Bengt Kasemo. Qcm operation in liquids: An explanation of measured variations in frequency and q factor with liquid conductivity. *Analytical Chemistry*, 68(13):2219 – 2227, 1996.

[62] David P. Morgan. *Surface-Wave Devices for Signal Processing*. Elsevier Science Publishing Company, Inc., paperback edition, 1991.

[63] R. Weigel, D.P. Morgan, J.M. Owens, A. Ballato, K.M. Lakin, K. Hashimoto, and C.C.W. Ruppel. Microwave acoustic materials, devices, and applications. *Microwave Theory and Techniques, IEEE Transactions on*, 50(3):738–749, 2002.

[64] T.W. Bristol, W.R. Jones, P.B. Snow, and W.R. Smith. Applications of double electrodes in acoustic surface wave device design. *1972 Ultrasonics Symposium*, pages 343–345, 1972.

[65] H. Engan. High-frequency operation of surface-acoustic-wave multielectrode transducers. *Electronics letters*, 10(19):395 – 396, 1974.

[66] Mats Jönsson. *Microfluidic Devices for Manipulation and Detection of Beads and Biomolecules*. PhD thesis, Uppsala University, Department of Engineering Sciences, 2006.

[67] R. Stoneley. Probation of elastic waves along the boundary of two solids. *Proceedings of the Royal Society of London*, 106:416 – 428, 1924.

[68] F. Petersson, A. Nilsson, C. Holm, H. Jonsson, and T. Laurell. Separation of lipids from blood utilizing ultrasonic standing waves in microfluidic channels. *Analyst*, 129(10):938–943, 2004.

[69] M. Wiklund and H. M. Hertz. Ultrasonic enhancement of bead-based bioaffinity assays. *Lab on a chip*, 6(10):1279 – 1292, 2006.

[70] J.J. Shi, X.L. Mao, D. Ahmed, A. Colletti, and T.J. Huang. Focusing microparticles in a microfluidic channel with standing surface acoustic waves (ssaw). *Lab on a chip*, 8(1):221 – 223, 2008.

[71] C. D. Wood, S. D. Evans, J. E. Cunningham, R. O'Rorke, C. Walti, and A. G. Davies. Alignment of particles in microfluidic systems using standing surface acoustic waves. *Applied Physics Letters*, 92(4), 2008.

[72] T. Irino, T. Watanabe, and Y. Shimizu. Zero slope temperature sio2/litao3structure substrate for stoneley waves. *IEEE Ultrasonics Symposium*, pages 257–260, 1987.

[73] T. Irino and Y. Shimizu. Optimized stoneley wave device by proper choice of glass overcoat. *Ultrasonics, Ferroelectrics and Frequency Control, IEEE Transactions on*, 36(2):159–167, 1989.

[74] Y. Shimizu and T. Irino. Stoneley waves propagating along an interface between piezoelectric material and isotropic material. *Ultrasonics Symposium*, pages 373–376, 1983.

[75] C. Iliescu, B. Chen, and J. Miao. Strategies in deep wet etching of pyrex glass. *Proceedings of the IEEE International Conference on Micro Electro Mechanical Systems (MEMS)*, pages 393–396, 2007.

[76] C. Iliescu, J. Jing, F. Tay, J. Miao, and T. Sun. Characterization of masking layers for deep wet etching of glass in an improved hf/hcl solution. *Surface and Coatings Technology*, 198(1-3):314–318, 2005.

[77] C. Iliescu, F. Tay, and J. Miao. Deep wet etching-through 1mm pyrex glass wafer for microfluidic applications. *Sensors & Actuators, A: Physical*, 133(2):395–500, 2007.

[78] D. Gachon, H. Majjad, W. Daniau, V. Laude, and S. Ballandras. Excitation of acoustic waves at the interface between lithium niobate and silicon plates. *Frequency Control Symposium, 2007 Joint with the 21st European Frequency and Time Forum IEEE International*, pages 733–736, 2007.

Acta Universitatis Upsaliensis

Digital Comprehensive Summaries of Uppsala Dissertations from the Faculty of Science and Technology 631

Editor: The Dean of the Faculty of Science and Technology

A doctoral dissertation from the Faculty of Science and Technology, Uppsala University, is usually a summary of a number of papers. A few copies of the complete dissertation are kept at major Swedish research libraries, while the summary alone is distributed internationally through the series Digital Comprehensive Summaries of Uppsala Dissertations from the Faculty of Science and Technology. (Prior to January, 2005, the series was published under the title "Comprehensive Summaries of Uppsala Dissertations from the Faculty of Science and Technology".)

Distribution: publications.uu.se
urn:nbn:se:uu:diva-100381

ACTA
UNIVERSITATIS
UPSALIENSIS
UPPSALA
2009